Investigating the Pollutant Formation and Combustion Characteristics of Biofuels in Compression Ignition Engines: A Numerical Study

Filip Jurić[a,*], Manuel Krajcar[a], Neven Duić[a], Milan Vujanović[a]

[a] University of Zagreb, Faculty of Mechanical Engineering and Naval Architecture, Ivana Lučića 5, 10000 Zagreb, Croatia

[*]Corresponding author e-mail: filip.juric@fsb.hr

ABSTRACT

In an effort to reduce carbon dioxide emissions, carbon-neutral biofuels are gaining attention as alternatives to fossil fuels. Biofuels produced from non-edible and algal biomass, which have combustion properties similar to conventional fuels and can be used in existing internal combustion engines, are one such fuel. This research employs numerical analysis to examine the combustion and pollutant formation characteristics of various biofuel generations, including biodiesel from coconut oil, waste coffee grounds, tomato seeds, and microalgae. The combustion process was modelled using the computational fluid dynamics software AVL FIRE™ and biofuel chemical mechanism from the University of Connecticut and validated on experimental results in internal combustion engine. The simulation conditions were evaluated based on an internal combustion operating point, with spray injection modelled using the Euler Lagrangian spray approach and liquid properties defined by the biofuel's saturated and unsaturated components. By altering the biodiesel/diesel mixture content, the results of in-cylinder pressure, temperature, rate of heat release, and pollutant emissions were compared to those of conventional fuel. Upon comparison of the conventional fuel with fixed released heat, a decrease of 4.6% and 1.2% in nitrogen oxides (NO) was observed for a mixture of 20% biodiesel (B20) and 50% (B50), respectively. The highest concentration of nitrogen oxide (NO) was found on the outer edges of the cylinder wall, however, due to more intense combustion, NO was more uniformly dispersed within the cylinder than diesel fuel and B20 with lower fuel injection.

KEYWORDS

Biofuel, emission, nitrogen oxides, combustion, spray, chemical mechanism

NOMENCLATURE

Label	Unit	Description
A		Pre-exponential factor in Arrhenius law
A_S	m^2	Surface area

* Corresponding author

C		Model constant
c	kmol/m^3	Concentration
D	m	Droplet diameter
D_k	m^2/s	Diffusion coefficient
E	J/kg	Activation energy
e	J/kg	Specific energy
F_d	N	Drag force
f		Fuel mixture fraction
f_i	m/s^2	Resulting volume force
g		Residual gas mass fraction
k	m^2/s^2	Turbulent kinetic energy
k		Global reaction rate coefficient
L	m	Turbulence length scale
M	kg/kmol	Molar mass
P_k	m^2/s^3	Production of turbulent kinetic energy
p	Pa	Pressure
q	W/kg	Specific heat
R	J/molK	Ideal gas constant
r	m	Droplet radius
S_k		Source term
t	s	Time
T	K	Temperature
T	s	Turbulence time scale
u	m/s	Velocity
x_i	m	Coordinates
y		Mass fraction
α	W/m^{2}K	Coefficient of convective heat transfer
β		Coefficient in Arrhenius law
Γ	m^2/s	Diffusion coefficient
ε	m^2/s^3	Turbulent energy dissipation rate
ζ	m/s	Velocity scale ratio
κ		Chemical symbol for species k
Λ	m	Wave length
λ	W/mK	Thermal conductivity
μ	Pas	Dynamic viscosity
μ_t	Pas	Turbulent viscosity
ν		Stoichiometric coefficient
ρ	kg/m^3	Density
Σ	1/m	Flame surface density

σ_{ji}	N/m^2	Stress tensor
τ	N/m^2	Viscous stress
τ_a	s	Break-up time
υ	m^2/s	Kinetic viscosity
Ω	s	Wave growth rate
ω	kg/m^3s	Combustion source

ABBREVIATIONS

BC	Boundary Condition
B20	20%−80% Biodiesel/diesel blend
B50	50%−50% Biodiesel/diesel blend
CA	Crank Angle
CFD	Computational Fluid Dynamics
CPU	Central Processing Unit
D100	100% Diesel fuel
ECFM-3Z	Three-zone Extended Coherent flame model
FAME	Fatty Acid Methyl Ester
GGPR	General Gas Phase Reactions
ICE	Internal Combustion Engines
IPCC	Intergovernmental Panel on Climate Change
LHV	Lower Heating Value
LLNL	Lawrence Livermore National Laboratory
MD	Methyl decanoate
MD9D	Methyl-9-decenoate
PM	Particulate Matter
RoHR	Rate of Heat Release
WCGO	Waste Coffee Ground Oils
0D	Non-Dimensional
3D	Three-Dimensional

1. INTRODUCTION

As the number of restrictions on the transport sector is rising every day due to the significant influence of Internal Combustion Engines (ICE) emissions on the environment, diverse fuel types are being researched to replace or lower the usage of fossil fuels [1]. Many pollutants are emitted from in-cylinder combustion in compression ignition engines, such as carbon dioxide (CO_2), particulate matter (PM), nitrous oxides (NO_x), and sulphides [2]. An answer to reducing net emissions from diesel fuel combustion is the development of new "environmentally friendly" fuels, such as biodiesel [3]. Biodiesel consists of long-chain fatty acid esters derived from various vegetable oils and animal fats by transesterification [4]. It is a chemical process that converts fats (triglycerides) found in oils and fats from feedstock into biodiesel andlycerol as a by-product [5]. Biodiesel, and biofuels in general, can be classified into four generations based on their biomass feedstock. First-generation biofuels

are produced from food crops and edible biomass. Second-generation biofuels are fuels produced from various non-edible feedstock such as agricultural residue, industrial waste, and waste cooking oil, which benefit of second-generation biofuels is their sustainability [6]. Third-generation biofuels are produced from algal biomass. Algal biofuels have numerous benefits compared to the first two generations of biofuels, such as growth in high CO_2 concentrated areas, higher oil yield, growth in wastewater, and challenging conditions meaning they do not need cultivable land [7]. Therefore, they do not interfere in food production. In [8], the authors compared microalgae biodiesel (Chaetoceros gracillis) to soybean biodiesel and standard diesel. Their results showed lower CO, hydrocarbons, and NOx emissions than conventional diesel fuel. Also, Rahman et al. showed that low volatility, high boiling point, density, and viscosity increase particle emission from microalgae biodiesel [9]. Studies have shown that biodiesel utilisation shows a decrease in hydrocarbons, carbon monoxide (CO), and PM, with a drawback in an increase in NO_x production [10]. However, other researchers showed that the increase in NO_x is mainly due to biodiesel fuels used in unmodified compression ignition engines [11].

Over the years, technological improvements have made it possible to numerically simulate combustion processes in ICE using Computational Fluid Dynamics (CFD) [12]. Numerical simulations have been widely used in engineering design and development [13]. By combining CFD analysis with experimental research, understanding complex and transient flow during the combustion process can be improved, which can result in a reduction of development costs [14]. Various fuels and fuel blends can be investigated and their influence on the combustion process in ICE using CFD analysis compared to the real-life experiments that are expensive and complex due to the consistency of operational parameters [15]. Moreover, CFD has proved to be very helpful for in-cylinder pollutant emission analysis, as an adequate support for the experimental research [16].

Recently, various publications on biodiesel and biodiesel blends have been published. For instance, CFD software AVL FIRE™ was combined with CHEMKIN code to analyse biodiesel-ethanol blends with various ethanol properties in a diesel engine [17]. Results showed a reduction of pressure inside the cylinder and thermal efficiency with increased ethanol share. The combustion analysis of sunflower and canola oil biodiesel was investigated in the same software and with similar models [18]. The combined non-dimensional (0D) chemistry with AVL FIRE™ has been applied for predicting pollutant emissions of various diesel-biodiesel blends [19], and e-fuels [20]. The results showed a decrease in pollutant emissions such as PM, CO, hydrocarbon, and NO_x, which confirms the positive influence of biodiesel in ICE. A new procedure optimizing pollutant emission, especially soot, was implemented by Arad et al. [21]. Additionally, a comparison between diesel and biodiesel blends was deeply investigated, and the results showed a decrease in NO_x emissions in the diesel-biodiesel fuel blends [22]. In [23], the authors compared various sunflower biodiesel and diesel blends (D100, B10, B20, and B100) inside a single-cylinder heavy-duty engine. Results showed lower combustion intensity for biodiesel, affecting the Rate of Heat Release (RoHR). However, an average reduction in NO_x, CO, and hydrocarbon emissions of 4%, 8%, and 20% was achieved. The second biodiesel generation combustion

and pollutant formation is also researched for waste cooking oil [24], and animal fat [25], where both showed a good potential for diesel substitution. Combustion and emission characteristics of biodiesel-diesel blends in a four-stroke diesel engine were investigated in [26], where the authors combined CFD software with CHEMKIN code to simulate the injection and combustion of various fuel mixes. Biodiesel combustion was simulated by a reduced kinetic mechanism consisting of 106 species and 263 reactions. Results showed an increase in NO_x emission with a higher biodiesel share. Compared to diesel, an increase of 9%, 18%, and 27% was obtained for B10, B20, and B30, respectively. The overall model predicted less soot formation and higher combustion temperatures than diesel fuel, which agreed with the experimental results.

The effect of low-temperature biodiesel combustion was investigated in [27], where the NO_x emission showed a completely different trend for biodiesel blends measured under different loads. In addition, the emission of syngas and biodiesel were also investigated in a compression engine powered in the dual fuel mode [28,29]. Combustion was analysed using the Extended Coherent Flame Model-3Z (ECFM-3Z), which accounts for the spray particles model, fuel disintegration and evaporation model, combustion, and the chemical model for pollutant production. A higher syngas percentage showed decreased combustion efficiency but higher thermal efficiency.

In order to describe the combustion of each biofuel, a chemical mechanism is crucial. As a result, detailed reaction mechanisms of numerous types of fuels, such as gasoline, jet, and diesel, contain many species and reactions [30]. Despite rapid progress in computing power, applying these detailed mechanisms to computational simulations regarding the Central Processing Unit (CPU) time and memory requirements is still challenging. Therefore, special attention will be paid in the following paragraph to finding a chemical mechanism suitable for describing different biofuels based on their chemical composition.

The reduction of complex mechanisms without impairing the computational fidelity is necessary to have applicable CFD solutions in real-time. The authors in [30]reduced various fuel mechanisms, resulting in a skeletal mechanism for biodiesel consisting of 177 species and 2904 reactions. Results for ignition delay times showed a great match with the experimental data. In [31], a discrete-component evaporation model was developed for biodiesel-diesel spray combustion. The model was paired with a reduced kinetic mechanism consisting of 95 species and 257 reactions and a multi-step soot model.

Several authors performed mechanism reduction from a detailed kinetic mechanism consisting of 3299 species and 10806 reactions made by Lawrence Livermore National Laboratory (LLNL). In [32], the authors developed a reduced biodiesel mechanism, which can be used in numerical studies of biodiesel applications. The mechanism was reduced to 156 species and 589 reactions. Results showed close agreements between the two mechanisms in ignition delay predictions, a trace of mixture temperature, and species mole fraction. Additionally, researchers [33] reduced the mechanism to 115 species and 460 reactions. The mechanism was validated against 0D simulations with detailed mechanism and experimental data. The reduced mechanism obtained a good prediction of combustion characteristics such as ignition delay, flame lift-off length, and equivalence ratio. Additional

mechanisms have been developed for special purposes, such as for homogeneous charge compression ignition engines [34], and moderate or intense, low-oxygen dilution combustion [35].

In [36], authors managed to reduce a detailed chemical mechanism for biodiesel obtained from LLNL. Starting mechanism consisted of 3299 species, and it was reduced to only 69 species making it usable for a three-dimensional (3D) CFD analysis in ICE. Biodiesel in the LLNL mechanism was described by two fuel surrogates, methyl decanoate (MD) and methyl-9-decenoate (MD9D), capable of representing the saturated and unsaturated methyl ester components of real biodiesel fuel, but also as diesel fuel. As a result of that, that mechanism is applied to all analysis in this paper.

The aim of this paper is to perform a 3D CFD comparative analysis of the engine combustion process and pollutant formation of the various generations of biodiesel using the exact general biodiesel mechanism and general gas-phase reactions (GGPR) approach. Among numerous published biofuel research, there is little, if any, accessible research on the extensive 3D evaluation of compression ignition engine performance, combustion, and emission characteristics of biodiesel from edible and non-edible oils biodiesel calculated with chemistry kinetics. Similar research, but for 0D simulations, was performed by [37], therefore, this study gives a valuable 3D insight into biodiesel combustion and pollutant formation. Biodiesel from coconut oil, waste coffee grounds, tomato seeds, and microalgae were observed, whose chemical composition is defined by altering the biodiesel Fatty Acid Methyl Ester (FAME) composition in the general chemical mechanism. Regarding the spray modelling, the liquid properties of biodiesel are modelled via user function in CFD software AVL FIRE™. The influence of different biodiesel-diesel blends on engine operating parameters like cylinder pressure, temperature, RoHR, and pollutant emissions is analysed.

2. MATHEMATICAL MODEL

Fundamental equations of continuum mechanics based on mass, momentum, and energy conservation laws are applied in this work. In the following section, models used to describe the process of combustion and heat release, such as turbulence, spray, and brake-up model, will be written out.

2.1. Species mass ratio conservation equation

In the combustion process, the conservation equations for each of the chemical species of interest are required. Opposite to the mass conservation equation, the source of chemical species inside the control volume can exist. For example, the source of chemical species from chemical reactions. The integral form of energy conservation equation can be expressed as:

$$\int_V \frac{\partial}{\partial t}(\rho y_\mathrm{k})dV + \int_S \rho y_\mathrm{k} u_i n_i dS = \int_S \rho D_\mathrm{k} \frac{\partial y_\mathrm{k}}{\partial x_i} n_i dS + \int_V S_\mathrm{k} dV \quad (1)$$

where y_k is the mass fraction of the chemical species k (k is not notation index). The term y_k is defined as the ratio between the mass of chemical species k and total mass.

$$y_{\mathrm{k}} = \frac{m_{\mathrm{k}}}{m_{\mathrm{total}}} \tag{2}$$

The left-hand side terms are analogous to the terms found in the mass conservation equation. The first term on the right-hand side of Eq(1) is the diffusion term. The diffusion term is modelled by Fick's law. Furthermore, in the diffusion term, constant D_k is called diffusion coefficient, and it is an analogue to thermal conductivity coefficient in heat and mass transfer analogy.

2.2. Turbulence modelling

One of the essential predictions in engineering problems is efficient turbulent flow modelling. Fluid flow in ICE is considered turbulent due to its characteristically swirling flows. Therefore, an adequate turbulence model needs to be applied. The *k-zeta-f* model is generally used in ICE simulations and was developed by Hanjalić et al. [38]. Thus, it was chosen as a turbulence model for this work. Some benefits of *k-zeta-f* turbulence model are improving the numerical stability of the model, especially when using segregated solvers. Due to the wall boundary condition for the elliptic function *f*, it is more robust and less sensitive to nonuniformities and clustering of the computational grid by applying a quasi-linear pressure–strain model in the equation of *f*. Another benefit is tolerance on small values of *y*+ in the wall-nearest cell center."

2.2.1. The k-zeta-f model

The model aims to improve the stability of the original $\overline{v^2} - f$ model by solving a transport equation for the velocity scale ratio $\zeta = \overline{v^2}/k$ instead of the velocity scale $\overline{v^2}$. The turbulent viscosity is obtained from:

$$\nu_t = C_\mu \zeta \frac{k^2}{\varepsilon} \tag{3}$$

Where C_μ is model constant, ζ is velocity scale ratio, k is turbulent kinetic energy and ε is the rate of turbulent energy dissipation.

Turbulent kinetic energy equation:

$$\rho \frac{Dk}{Dt} = \rho(P_k - \varepsilon) + \frac{\partial}{\partial x_j}\left[\left(\mu + \frac{\mu_t}{\sigma_k}\right)\frac{\partial k}{\partial x_j}\right] \tag{4}$$

Turbulent energy dissipation rate:

$$\rho \frac{D\varepsilon}{Dt} = \rho \frac{(C^*_{\varepsilon 1} P_k - C_{\varepsilon 2}\varepsilon)}{T} + \frac{\partial}{\partial x_j}\left[\left(\mu + \frac{\mu_t}{\sigma_k}\right)\frac{\partial \varepsilon}{\partial x_j}\right] \tag{5}$$

Velocity scale ratio:

$$\rho \frac{D\zeta}{Dt} = \rho f - \rho \frac{\zeta}{k} P_k + \frac{\partial}{\partial x_j}\left[\left(\mu + \frac{\mu_t}{\sigma_\zeta}\right)\frac{\partial \zeta}{\partial x_j}\right] \tag{6}$$

Elliptic relaxation function f can be written:

$$f - L^2 \frac{\partial^2 f}{\partial x_j \partial x_j} = \left(C_1 + C_2 \frac{P_k}{\varepsilon}\right) \frac{\left(\frac{2}{3} - \zeta\right)}{T} \tag{7}$$

Turbulent time scale T and length scale L are given by:

$$T = \max\left(\min\left(\frac{k}{\varepsilon}, \frac{a}{\sqrt{6}C_\mu |S|\zeta}\right), C_T \left(\frac{\upsilon}{\varepsilon}\right)^{\frac{1}{2}}\right) \tag{8}$$

$$L = C_L \max\left(\min\left(\frac{k^{\frac{3}{2}}}{\varepsilon}, \frac{k^{\frac{1}{2}}}{\sqrt{6}C_\mu |S|\zeta}\right), C_\eta \frac{\upsilon^{\frac{3}{4}}}{\varepsilon^{\frac{1}{4}}}\right) \tag{9}$$

2.3. Spray modelling

Spray modelling is crucial for accurately describing mixing, ignition, combustion, and emission processes occurring in ICE. It describes multi-phase flow and requires solving conservation equations for both the liquid and the gas phase simultaneously. The method used to solve practically all spray calculations in engineering problems today is called discrete droplet method or the Euler Lagrangian method. The method approximates spray droplets as groups of droplets (parcels) that exhibit the same properties. The liquid phase is calculated using the Lagrangian conservation equation, while the gas phase is described using the Eulerian approach.

Essential sub-models used in biodiesel injection are:

- Break-up model → Wave
- Evaporation model → Dukowicz
- Turbulence dispersion model
- Drag law model → Schiller-Naumann
- Wall interaction model → Walljet1

In this work, the following assumptions are defined for spray modelling:

- The spherical symmetry of droplets
- Quasi-steady gas film around the droplet
- Uniform droplet temperature at the drop diameter
- Uniform physical properties of the surrounding fluid
- Liquid-vapour thermal equilibrium on the surface of the droplet

The interaction between the discrete liquid phase and gaseous phase is modelled by evaporation model, where the sink of liquid mass is modelled as the source term in the evaporated fuel species transport equation in a gaseous phase [39].

2.4. Combustion modelling

In this paper, combustion modelling was performed via a chemical mechanism. Each fuel has its specific set of chemical reactions describing the combustion process. Chemical mechanism consists of elementary chemical reactions for each species individually.

The reaction rates are calculated in the general form:

$$\sum_{k=1}^{K} \nu'_{ki} \kappa_k \Leftrightarrow \sum_{k=1}^{K} \nu''_{ki} \kappa_k \ \ (i = 1, \dots, I) \tag{10}$$

Where ν represents stoichiometric coefficients of the reactants and products and κ is the chemical symbol for the species k.
The stoichiometric coefficient of species k in reaction i is defined as:

$$\nu_{ki} = \nu'_{ki} - \nu''_{ki} \tag{11}$$

The species production rate k ($\dot{r}_k$) is defined as:

$$\dot{r}_k = \sum_{i=1}^{I} \nu_{ki} \, \dot{q}_i \tag{12}$$

while the reaction rate $\dot{q}_i$ of reaction is defined by the difference of forward and backward reaction rates:

$$\dot{q}_i = k_{f_i} \prod_{k=1}^{K} \left[c_{k,g}\right]^{\nu'_{ki}} - k_{r_i} \prod_{k=1}^{K} \left[c_{k,g}\right]^{\nu''_{ki}} \tag{13}$$

Where $c_{k,g}$ represents the molar concentration of species k.
The source term S_k from the Equation (4) describing the species mass conservation can be modelled according to the Arrhenius law:

$$k = AT^{\beta} \exp\left(-\frac{E}{RT}\right) \tag{14}$$

Where k is the global reaction rate coefficient, and E represents activation energy. The coefficients A, β and E are determined from experimental data. The coefficients A, β and E represent the pre-exponential factor, temperature dependence factor and activation energy. In this approach, the burning rate depends on the chemical kinetics while turbulent fluctuations are ignored. Inside the chemical reactions, species can originate as products or reactants. If the species is modelled as a reactant, it will be modelled as a sink in its transport equation. The volume source S_k for a chemical species is expressed as a difference between all forward and backwards reactions, considering the concentration of chemical species in these reactions:

$$S_{\mathrm{k}} = \frac{dc_k}{dt} \cdot M_k = \sum_{1}^{m} k_{m,f} \cdot c_m \cdot c_{oxy} - \sum_{1}^{n} k_{n,b} \cdot c_n \cdot c_{red} \tag{15}$$

Index m represents the total number of forward reactions in which the chemical species is a product, and index n means the total number of backward reactions in which the chemical species is a reactant. Species transport was modelled inside GGPR, where calculates Equation (1) is calculated for each chemical species k. Additionally, gaseous media is assumed to be the ideal gas.

3. NUMERICAL SETUP

This chapter will overlook the entire parameters necessary for CFD simulation, from the mesh, time step discretisation, boundary and numerical setup, spray setup and injection rates, and the combustion model.

3.1. Engine and mesh information

The engine used for biodiesel combustion analysis is a Single CYlinder ENgine (SCYLEN), equipped with electro-hydraulic valve actuation and a ω−shaped piston. Engine specifications are found in Table 1:

Table 1: Engine specifications

Engine data		Injector data	
Bore	85 mm	Number of nozzle holes	8
Stroke	94 mm	Spray cone angle	158°
Compression ratio	16:1	Injection pressure	1200−1600 bar
Nozzle location	3.8 mm	Nozzle diameter	0.1 mm
Displacement	533.4 mm^3		

The computational mesh used in this work contains two boundary layers surrounding the combustion chamber and a compensation volume at the piston rim. Due to axial symmetry, the mesh covers only a volume around one nozzle, and since the injector contains eight nozzles, only 1/8 of the cylinder volume was used, as seen in Figure 1. The mesh passed all the checks, and it has zero negative and non-orthogonal cells. Cell information is shown in Table 2.

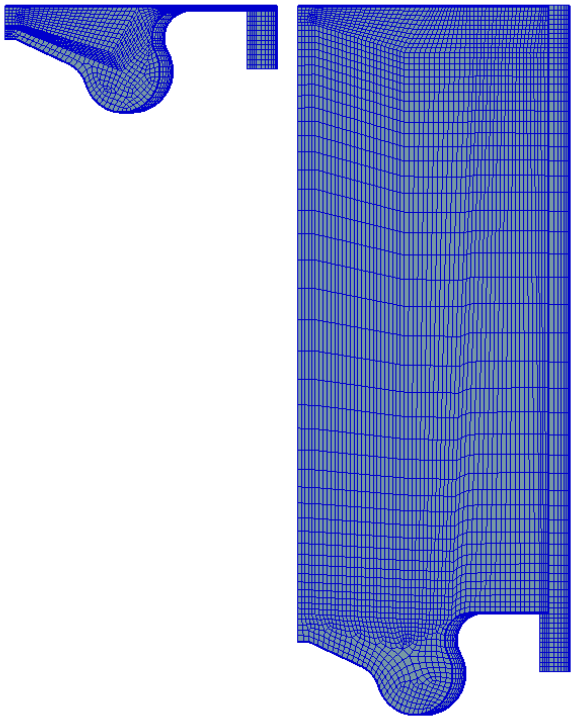

Figure 1: Mesh topology at TDC and BDC

Table 2: Mesh information for TDC and BDC

	TDC	BDC
Volume	4.44 cm^3	71.09 cm^3
Number of cells	23834	67558
Compression ratio	16.01	

3.2. Time discretisation

The run time for the combustion analysis was set in crank-angles (CA). The intake and the exhaust valve were closed during the working cycle period. The start angle was set to 606 CA, and the end angle point was defined at 860 CA. Full-time step is shown in Table 3.

Table 3: Simulation time step

Up to Crank-Angle, CA	Time step, CA
611	0.1
618	0.5
695	1
709	0.5
740	0.1
820	0.5

834	1
860	2

A smaller time step was used at the beginning of the simulations and during the fuel injection to acquire numerical stability.

3.3. Boundary conditions

Boundary conditions (BC) for the volume mesh were defined via boundary face selections. For every operating point, the same BC was used. Constant temperature BC was used for the cylinder head, the piston, and the liner. Symmetry BC is used for the axis. Since 1/8 of the volume was used, the segment boundary was periodic on both sides of the mesh as shown in Figure 2. At the compensation volume walls, an adiabatic boundary condition was used. The piston wall temperature is obtained from the cooling oil temperature, and the head wall is obtained from the measured temperature of cooling water. The experimental data was inherited from previous research [40].

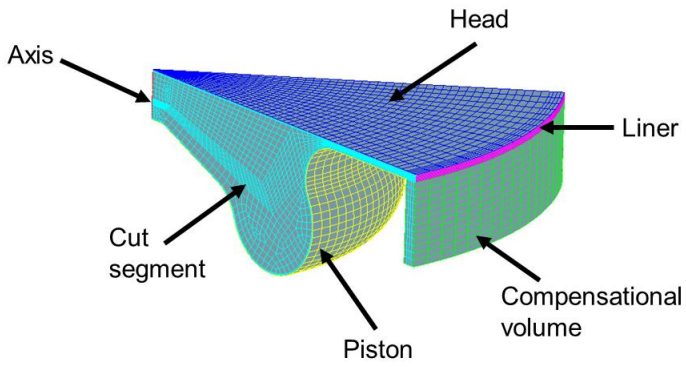

Figure 2: Computational mesh with defined selections

Table 4: Boundary conditions

Face	Boundary condition
Piston	Type: Wall Temperature: 550 K
Liner	Type: Wall Temperature: 410 K
Axis	Type: Symmetry
Cut segment	Type: Inlet/Outlet, Periodic
Compensation volume	Type: Wall Heat flux: 0 W/m^2
Head	Type: Wall Temperature: 500 K

3.4. Initial conditions

Pressure, density, temperature, swirl, and initial gas composition in ICE must be set. When modelling combustion with General Gas Phase Reactions (GGPR), exact mass fractions of

each species can be set. Initial values were used from acquired experimental data. The initial values are shown in Table 5. The selected cases feature a low content of recirculated exhaust gases, high oxygen concentration, and high swirling, which also ensures the exhaustion of burnt fuel gasses. The ICE simulation was only observed for the operating cycle when the intake and exhaust valves are closed and when is no mass transfer with the intake and exhaust system. All measurement values are averaged for 100 measurement cycles. The air temperature entering the intake manifold is at the ambient temperature, which is then increased due to the compression inside the cylinder and burnt gasses. When the intake valve is closed, the initial temperature is measured.

Table 5: Initial conditions

	Case 1	Case 2	Case 3	Case 4
Pressure, Pa	251800	252600	237700	241300
Density, kg/m^3	2.08	2.08	1.99	2.00
Temperature, K	423	425	416	420
Swirl, 1/min	5403	6869	5723	7096
Mass fraction, kg/kg				
- O_2	0.2083	0.2038	0.2034	0.2128
- N_2	0.7631	0.7621	0.7621	0.7640
- CO_2	0.0196	0.0236	0.0239	0.0160
- H_2O	0.009	0.0105	0.0106	0.0072

3.5. Solver control

The under-relaxation factors ensure that the solution from one step to the next does not change too much as it might get unstable. By lowering the under-relaxation factors, the solution changes very little from one step to the next, leading to a stable solution but prolonging the simulation time. On the other hand, if the under-relaxation factors are too high, the solution changes too much from one step to the next, leading to divergence. Under relaxation factors used in this paper are shown in Table 6.

Table 6: Under relaxation factors

Equations	
Momentum	0.6
Pressure	0.3
Turbulent kinetic energy	0.4
Turbulent dissipation rate	0.4
Energy	1
Mass source	1
Viscosity	1
Scalar	0.8
Species transport equation	0.8

Concerning the differencing schemes, an equal share combination of the central differencing and upwind scheme was used for the momentum equation. The central differencing scheme was used for the continuity equation, while the upwind scheme was used for turbulence, energy, and scalar transport equations. The solution converged when the pressure, momentum, and temperature normalised residual decreased under the 10^{-4}.

3.6. General Gas Phase Reactions

Chemical kinetic mechanisms are used to represent conventional and newly developed fuels in combustion devices like ICE [41]. The combustion process was modelled by the FIRE^{TM} General Gas Phase Reactions Module. This model enables various types of chemical kinetic problems in 3D CFD. As mentioned before, detailed chemical kinetic mechanisms have shown to be ineffective for 3D transient combustion analysis due to high computational necessities. Therefore, many researchers are performing reductions of these mechanisms to be implemented for 3D combustion analysis.

The kinetic mechanism used for biodiesel analysis in this paper was developed by [33], where the authors reduced a detailed mechanism developed by LLNL. LLNL created a detailed kinetic mechanism for biodiesel consisting of two surrogate species, methyl decanoate (MD) and methyl-9-decenoate (MD9D) [42]. The two surrogates can efficiently represent saturated and unsaturated methyl esters of biodiesel. Using various mechanism reduction methods, the authors reduced the mechanism from 3299 species and 10806 reactions to 115 species and 460 reactions, respectively. The Extended Zeldovich Model has used for the NO formation processor thermal NO emissions with the temperature fluctuations consideration [43].

3.7. Fuel composition

The biodiesel consists of multiple fatty acid methyl esters, of which five main esters are obtained from *Palmitic*, *Stearic*, *Oleic*, *Linoleic*, and *Linolenic* acid [44].

First, second, and third-generation biodiesels were analysed in this paper. Coconut oil represents the first-generation biofuel as it is considered an edible feedstock. Two second-generation feedstocks were analysed, waste coffee ground oils (WCGO) [45] and tomato-seed oils[46]. Third-generation biofuels are composed of microalgae feedstock. Spirulina microalga was analysed, and its composition was obtained from [47] [48]. Only the fatty acids with the highest share were considered for the combustion analysis, while the other acids with a negligibly small share were neglected. For WCGO, tomato seed oil, and spirulina microalgae, the highest percentage of fatty acid methyl esters have the previously mentioned *Palmitic*, *Stearic*, *Oleic*, *Linoleic,* and *Linolenic* methyl esters, while coconut oil has a high share of *Lauric* and *Myristic* fatty acids. The composition of the biodiesel is shown in Figure 3.

The exact fuel blend ratio and fuel composition have to be defined from the species found in the kinetic mechanism. As mentioned, the chosen mechanism represents FAME via the two surrogate species. The saturated FAMEs are represented by MD, and the unsaturated by MD9D, respectively. B100 and high-concentration FAME diesel blends cannot be used in ICE without a substantial risk of oil quality deterioration, clogging of particulate filters, and

dissolving materials [49]. Therefore, many world regions have limits on the maximum FAME concentration in diesel fuels, like Europe, in which the maximum FAME concentration in diesel is limited to 7%. Nevertheless, higher FAME concentrations can be used in fleet operations like city busses, taxis, or heavy-duty transport like trucks, tractors, and marine compression ignition engines. For this reason, higher FAME blends of B20 will be analysed in the single-cylinder engine. The composition of the B20 blend for the analysed feedstocks is shown in Table 7, and of the B50 blend in Table 8. Biodiesel liquid properties are described separately, implementing user functions. Implemented user functions contained the following properties:

- molecular weight (kg/kmol)
- diffusion volumes (-)
- critical temperature (K)
- critical pressure (Pa)
- melting point at atmospheric pressure (K)
- number of different molecular groups for UNIFAC
- molecular group identification for UNIFAC
- boiling point at atmospheric pressure (K)
- critical compressibility factor
- critical molar volume (cm^3/mol)
- liquid density (kg/m^3)
- liquid dynamic viscosity (kg/(m s))
- liquid specific heat (J/(kg K))
- surface tension (N/m)
- liquid thermal conductivity (W/(m K))
- latent heat of evaporation (J/(kg K))
- vapor pressure (Pa)

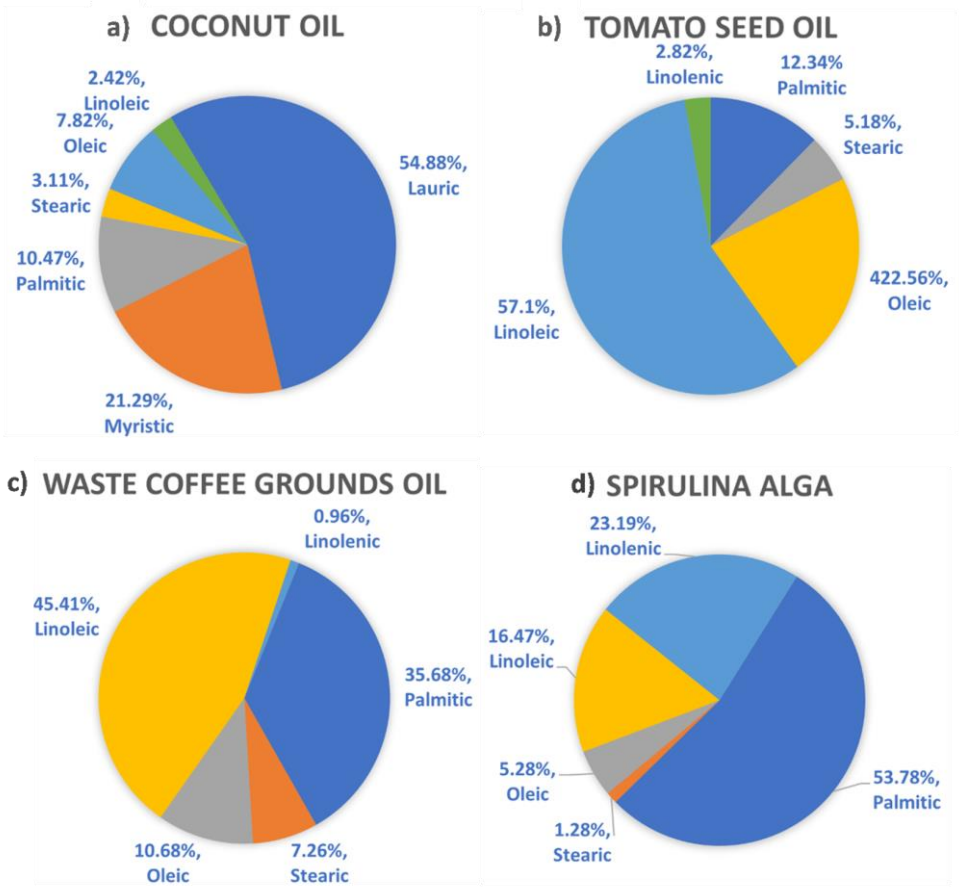

Figure 3: Volumetric composition of FAME in Coconut oil (Figure 3a), Tomato seed oil (Figure 3b), WCGO (Figure 3c), Spirulina microalga (Figure 3b)

Table 7: Mass fraction of B20 biodiesel-diesel blends

	Coconut oil			Tomato seed oil		
	x	Specie	x	x	Specie	x
Lauric	0.1742			/		
Myristic	0.0676	**MD**	**0.2849**	/	**MD**	**0.0558**
Palmitic	0.0332			0.0393		
Stearic	0.0099			0.0165		
Oleic	0.0246			0.017		
Linoleic	0.0076	**MD9D**	**0.0322**	0.1797	**MD9D**	**0.2596**
Linolenic	/			0.0089		
n-Heptane	0.6829	**nC7H16**	**0.6829**	0.6847	**nC7H16**	**0.6847**

	WCGO			Spirulina microalga		
	x	Specie	x	x	Specie	x
Palmitic	0.1134	**MD**	**0.1365**	0.1709	**MD**	**0.175**

Stearic	0.0231			0.0041		
Oleic	0.0336			0.0166		
Linoleic	0.1428	**MD9D**	**0.1794**	0.0518	**MD9D**	**0.1413**
Linolenic	0.003			0.0729		
n-Heptane	0.684	**nC7H16**	**0.684**	0.6838	**nC7H16**	**0.6838**

Table 8: Mass fraction of B50 biodiesel-diesel blends

	Coconut oil			Tomato seed oil		
	x	Specie	x	x	Specie	x
Lauric	0.3571			/		
Myristic	0.1385	**MD**	**0.584**	/	**MD**	**0.1146**
Palmitic	0.0681			0.0807		
Stearic	0.0202			0.0339		
Oleic	0.0504			0.1459		
Linoleic	0.0156	**MD9D**	**0.066**	0.3694	**MD9D**	**0.5336**
Linolenic	/			0.0182		
n-Heptane	0.35	**nC7H16**	**0.35**	0.3518	**nC7H16**	**0.3518**

	WCGO			Spirulina microalga		
	x	Specie	x	x	Specie	x
Palmitic	0.233	**MD**	**0.2804**	0.3508	**MD**	**0.3591**
Stearic	0.0474			0.0083		
Oleic	0.0690			0.034		
Linoleic	0.2932	**MD9D**	**0.3684**	0.1063	**MD9D**	**0.29**
Linolenic	0.0062			0.1496		
n-Heptane	0.352	**nC7H16**	**0.3512**	0.3509	**nC7H16**	**0.3509**

3.7.1. Spray setup

The temperature of the injected fuel was experimentally measured, and its value was set to 320 K. Spray angle, penetration, and injection properties were defined from a methodology developed in previous research [50].

Table 9 shows the injector data input necessary to perform numerical simulations. The spray delta angle 1 represents the double angle between the spray axis and the nozzle axis, while the half outer cone angle is defined as the angle between the nozzle hole axis and the widest parcel trajectory.

Along with all the necessary numerical setup, the following assumptions were made:

- Ideal gas properties for the components in the cylinder: Prandtl number, Pr=0.9m, Schmidt number, Sc=0.7
- Compressible flow
- Viscid fuel

- No interaction between the droplets

Table 9: Injector data

Position	(0, 0, -3.8) mm
Direction	(0, 0, 1)
Nozzle hole diameter	0.1 mm
Nozzle diameter at hole centre position	4 mm
Spray delta angle 1	158°
Half outer cone angle	7.5°

The amount of fuel and the beginning of injection for each case is shown in Table 10.

Table 10: Injection timing and amount of injected fuel

	Case 1	Case 2	Case 3	Case 4
Injected mass, μg	3.38	3.39	3.39	3.37
Injection timing, CA°				
Start	713.5	709.3	715.8	712.6
Stop	734.8	732.4	735.6	732.4

3.8. Mesh dependency test

Three different meshes with the same block structure were tested. Meshes varied in the number of cells due to different cell sizes. The meshes had dependent cell sizes where up until 29.2 CA°, cell sizes were smaller so that the proper representation of the phenomena happening in TDC can be explored. Later, for higher CA°, cell sizes were larger to shorten the computational time. The specifications of the analysed meshes are given in the following Table 11.

Table 11: Properties of analysed meshes

Mesh	Dependent cell size [mm]		No. of cells in TDC	No. of cells in TDC	No. of meshes
	0°CA	29.2°CA			
Coarse	0.6	1.2	23834	67558	23
Medium	0.5	1.0	49050	71775	23
Fine	0.4	0.8	65700	101150	23

The comparison of the meshes was performed on Case 3 operating point (defined in Table 5). The values of the in-cylinder mean pressure and the RoHR were observed. Obtained values are shown in

Figure 4 and Figure 5. It can be observed that there are minor differences in the tested meshes. There are no differences during the compression and expansion period. Also, the ignition delay time is precisely the same for all the meshes. The most significant difference

is in the peak values, where the coarse mesh shows slightly higher values than the fine and medium meshes, for which a negligible deviation was achieved. For this reason, in the following analysis, the medium mesh was used.

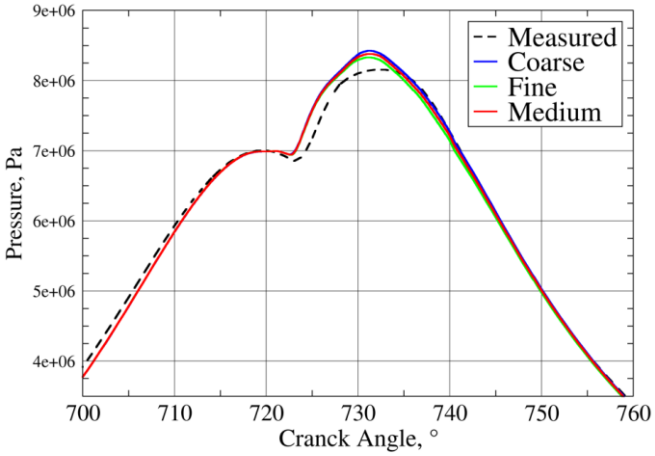

Figure 4: Cell size impact on in-cylinder mean pressure

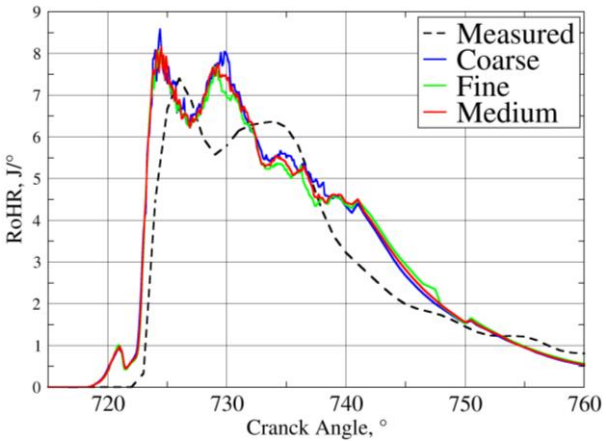

Figure 5: Cell size impact on RoHR values

4. RESULTS AND DISCUSSION

The primary task of this paper was to analyse the influence of biodiesel feedstocks and how their FAME composition influences combustion characteristics in compression ignition engines. All results shown in the following section are compared against measured experimental results from [40] performed for D100 fuel. In all graphs, the combined spray and chemical kinetic mechanism in this work are validated against experimental results, performing the simulations with D100 fuel used in the experiment. For the description of diesel combustion, chemical species n-heptane was applied. Due to the lack of experiments for biodiesel fuel, biodiesel blend results are then verified compared to D100 fuel, and between themselves. The previous chapter showed all the necessary input data and simulation setup, while in this chapter, the combustion characteristics like in-cylinder pressure, RoHR, internal temperature, and pollutant emissions will be observed.

4.1.B20 Blends

As can be seen in Table 7, the FAME composition of analysed biodiesel fuels varied depending on the plant-derived feedstock. For example, coconut oil is shown to have the highest share of shorter carbon chain saturated fatty acid, thus the highest MD concentration. Conversely, tomato-seed oil has an increased share of longer carbon chain unsaturated fatty acids. WCGO and Spirulina blends have an opposite share of FAME, meaning that the content of the saturated fatty acids of WCGO blends is like the unsaturated content of Spirulina blend.

Figure 6 shows the in-cylinder results for experimental data, D100, and B20 blends. From the validation of D100 with experimental data, the difference can be attributed to a smaller amount of injected fuel resulting in faster disintegration of the fuel spray and, thus, more rapid fuel evaporation. Due to the quicker fuel evaporation, the mixing process of evaporated fuel with air resulted in the earlier formation of the stoichiometric conditions, thus, earlier autoignition. Additionally, owing to the lower realized heat in CFD simulations than in the experimental setup, the peak values are decreased and achieved earlier. That is why the result with the same released heat will also be analyzed in the later subsection of the paper.

When comparing the experimental measures to the modelled D100 fuel, great accordance can be seen across all the operating points during the compression and expansion strokes. However, when ignition commences, D100 tends to ignite sooner and reaches higher pressure values. This can be attributed to D100 being depicted by surrogate n-heptane.

The obtained results of the pressure distribution inside the cylinder for B20 blends show lower pressure values for all the diesel-biodiesel mixtures compared to the conventional fuel. An approximate 5% reduction in peak pressure for B20 blends compared to D100 is obtained in Case 1. A comprehensive comparison between the analysed feedstock will be given for each case separately.

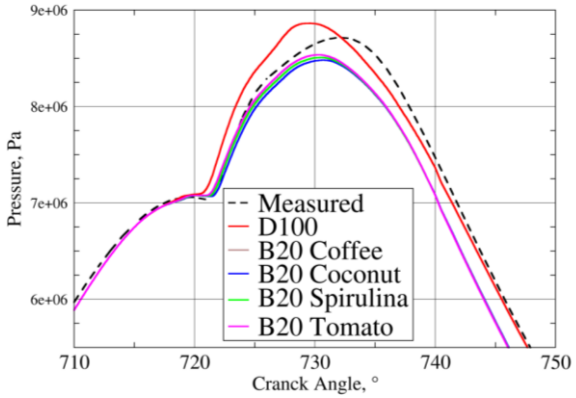

Figure 6: In-cylinder pressure distribution of B20 blends – Case 1

The identical trend in in-cylinder results is obtained when comparing the pressure values of different feedstock blends. The coconut blend ignited last during the ignition phase, while the tomato-seed mixture ignited first. Spirulina and WCGO blends are between the coconut and the tomato blends, with an almost equal composition of saturated and unsaturated FAME. Due to their similar MD and MD9D chemical species content, no significant

difference between the two feedstocks is observed, as their peak values and ignition delay time are practically identical. Behaviour in Case 1 can lead to the conclusion that the higher share of unsaturated fatty acids can lead to sooner ignitions and higher pressures. Moreover, FAME composition did not influence the in-cylinder pressure during the compression and expansion strokes.

When observing the mean temperature inside the cylinder in Figure 7, it can be observed that the mechanism obtained slightly higher values for D100 compared to the experiment. Earlier ignition of D100 is also visible. The mechanism also predicts higher post-combustion temperatures than the experimentally obtained values. For the B20 blends, as per pressure behaviour, no significant difference is observed between the blends. The decreased autoignition delay time of the tomato-seed mixture is also visible in the temperature curvatures. Overall, the combustion process has decreased duration with lower peak temperatures. The underprediction of B20 blends is achieved for approximately 60 K compared to the D100 results, and around 50 K for experimental data. Although the peak temperature between D100 and experimental data is achieved in the range of 20 K, their shift in peak values can be observed, which is obtained due to a more wide high-temperature region near the head wall, which is discussed in 3D results.

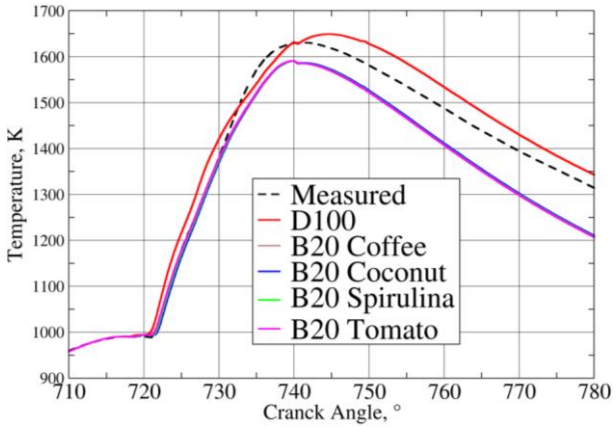

Figure 7: In-cylinder mean temperature – Case 1

Figure 8 shows RoHR results, where an agreement with the pressure inside the cylinder in Figure 6 is achieved. The values for D100 show rapid ignition at the beginning of the combustion, corresponding to higher pressure values. Although biodiesel blends do not have significantly different ignition results, the differences are discussed later in section 4.5. The tomato-seed oil blend has the shortest ignition delay, followed by the Spirulina and WCGO mixtures and coconut oil igniting the latest. The second characteristic peak of RoHR results, where CO is oxidizing, is achieved earlier in simulations compared to the measured data. This difference can only be attributed to the chemical mechanism and substitution of the diesel fuel chemical reaction pathway with n-heptane, which tends to react more quickly due to its shorter carbon chains.

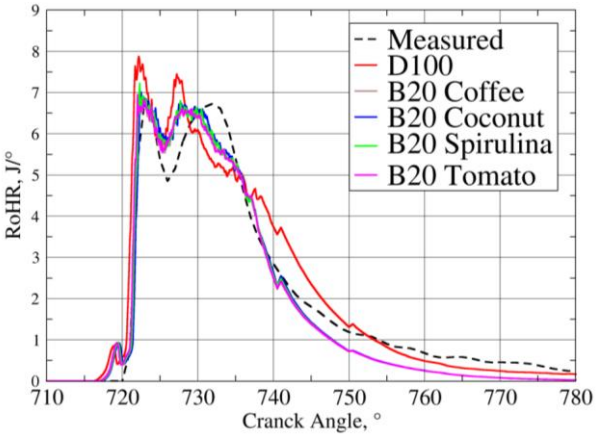

Figure 8: Rate of Heat Release for B20 blends – Case 1

Similarly, as shown in Case 1, in Figure 9, Case 2 showed an increase in peak pressure for the modelled D100 diesel compared to experimental values. Also, the ignition delay time was shorter due to the earlier injection. The combustion process is more intensive as the pressure gradient of the modelled diesel is significantly higher compared to Case 1. Same as in Case 1, validation of D100 showed over-prediction in the ignition, while the agreement with the experimental results is achieved in the expansion.

A 3% decrease in peak pressure is observed when analyzing the in-cylinder pressure of biodiesel blends in comparison to D100. The reduced difference in peak pressure between biodiesel blends and Case 1 may be attributed to a more robust swirling motion, resulting in superior fuel particle dispersion in the combustion chamber, leading to enhanced combustion. The feedstock analysis indicates that all three biodiesel blends perform similarly, indicating that the chemical structure's impact on biodiesel combustion performance is not substantial under higher swirl motion.

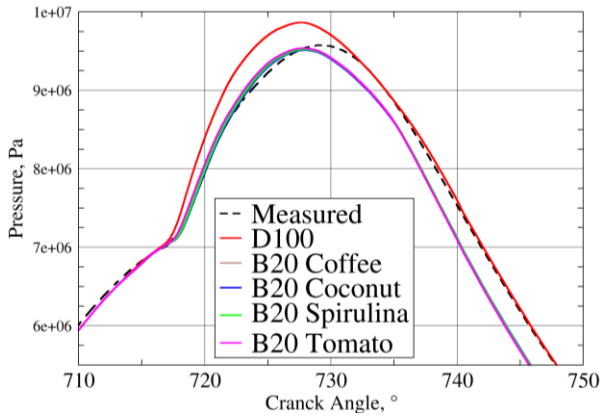

Figure 9: In-cylinder pressure distribution of B20 blends – Case 2

The mean in-cylinder temperatures are higher for D100 during the entire expansion stroke, which is shown in Figure 10. Moreover, compared to Case 1, the temperatures are higher for

all the B20 mixtures. This behavior can be attributed to the increased swirling motion, which enables the flame front to propagate more profoundly into the combustion chamber, facilitating heat transfer through convection and leading to improved combustion. In the case of early injection, the chemical mechanism employed exhibited the highest degree of deviation in the validation results. This observation can be ascribed to the heightened heat release in Case 2 (Figure 11) and the more noticeable differentiation between D100 and n-heptane combustion at lower temperatures, which is when the injection process began. The fast and intensive ignition in RoHR corresponds to higher values of pressure gradients in Case 2. The difference in biodiesel blends concerning the released heat is negligible, which is in accordance with pressure behaviour. Notably, in this instance, there was a poorer trend tracking of the second peak quantity of RoHR, which shares the same source of error as the temperature results presented earlier.

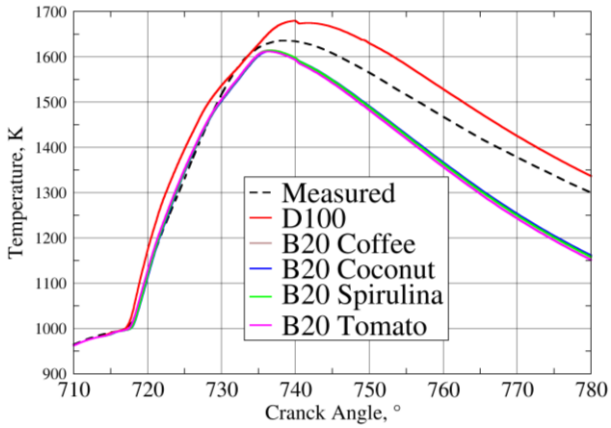

Figure 10: In-cylinder mean temperature – Case 2

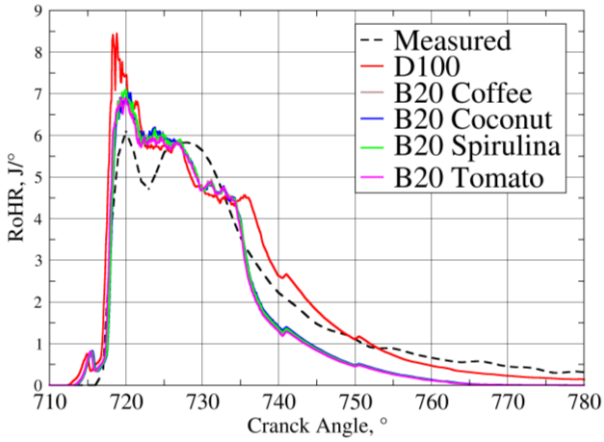

Figure 11: Rate of Heat Release for B20 blends – Case 2

Case 3 is noteworthy for its extended ignition delay times and the latest start of injection, shown in Figure 12, Figure 13, and Figure 14. As with all cases, the n-heptane surrogate in D100 exhibited a tendency to ignite sooner than the experimentally obtained values. When

comparing the biodiesel blends to D100, a 6% reduction in peak pressure was observed, with the tomato-seed blend exhibiting the highest pressure. Similar to Case 1, the influence of the chemical structure on the combustion performance of the biodiesel blends remained the same. The blends containing a higher proportion of unsaturated FAME ignited sooner and demonstrated a slightly higher peak pressure compared to those with a higher percentage of saturated FAME. In addition to the impact of chemical composition, Case 3 is notable for having the lowest pressure inside the cylinder prior to ignition, which in turn resulted in lower temperatures and even longer ignition delay times, as illustrated in Figure 12. The swirling motion values in Case 3 were not as high as in Case 2. Furthermore, less intense combustion occurred due to the lower in-cylinder temperature values. Following the behaviour of the previous cases, the temperature trend of biodiesel blends is preserved. The longer ignition delay time is more pronounced, but the biodiesel mixtures have no significant differences. The most significant differences among the biodiesel results are manifested in the pressure outcomes, with a notable discrepancy of 25 bars in peak pressure observed between the coconut and tomato biodiesel blends.

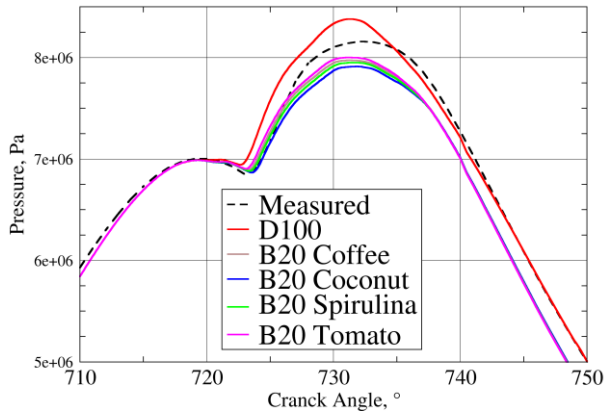

Figure 12: In-cylinder pressure distribution of B20 blends – Case 3

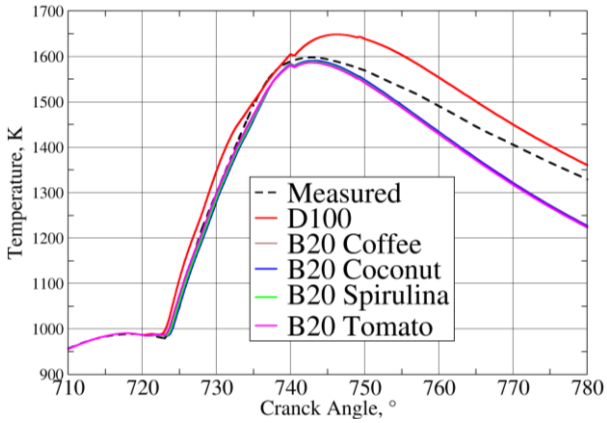

Figure 13: In-cylinder mean temperature – Case 3

Similar to Case 1, in Figure 14, D100 shows rapid ignition and higher peak values compared to the experimental values. Looking at the B20 blends, the peak RoHR values are obtained around 730 CA°. This behaviour is probably due to a much longer ignition delay compared to other cases. Also, looking at the released energy during the expansion cycle, a higher drop in the released energy is observed in all cases. Due to overall lower amounts of released energy, a lower pressure during the expansion cycle is observed for all biodiesel blends.

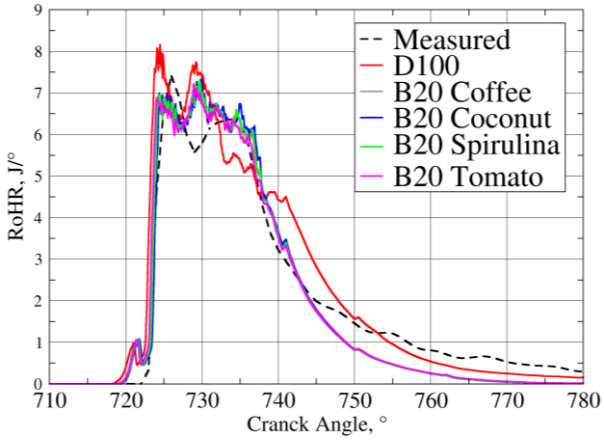

Figure 14: Rate of Heat Release for B20 blends – Case 3

D100 demonstrated a considerably steeper pressure gradient for the fourth operating point; however, its peak value was much closer to the measured data. B20 blends exhibited a reduction of approximately 3.5% in peak pressure, providing evidence that higher swirling motion cases lead to improved combustion performance. A comparison of the initial conditions of Case 4 and Case 2 revealed that both cases exhibited high initial pressure and swirl values. Nevertheless, due to the slightly higher-pressure values observed in Case 2 (as shown in Figure 15), an increased pressure gradient and decreased ignition delay times were observed. The chemical composition exhibited little to no influence on combustion performance under high swirl conditions.

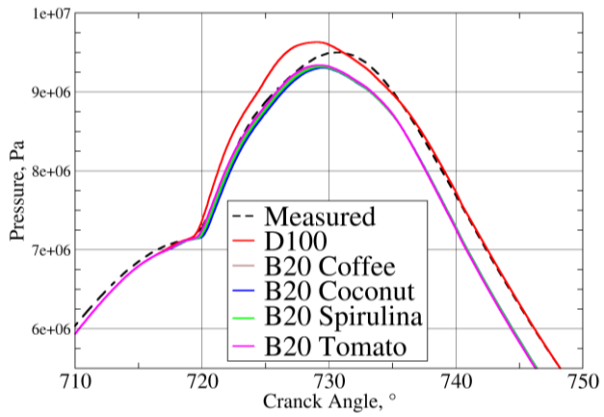

Figure 15: In-cylinder pressure distribution of B20 blends – Case 4

Similarly to Case 2, due to higher swirling motion, the ignition delay times for all mixtures are practically the same. The D100 fuel still shows a slightly higher temperature gradient and overpredicted peak values than the measured values.

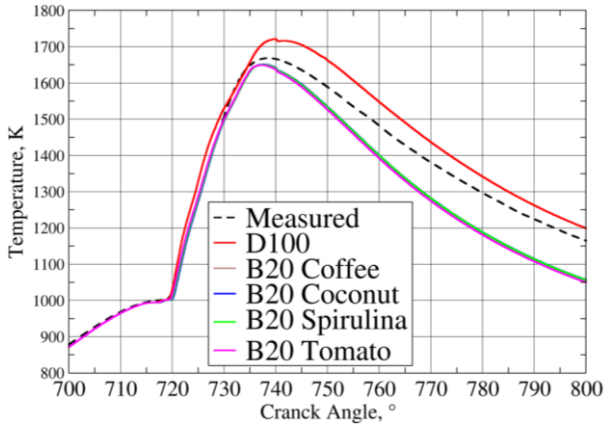

Figure 16: In-cylinder mean temperature – Case 4

In Figure 17, D100 shows an overpredicted peak value during ignition, which correlates to the overpredicted pressure gradient in Figure 15. Meanwhile, all the blends show similar behaviour throughout the combustion process. When compared to Case 2, higher peak values are observed. This behaviour is due to higher initial oxygen content in Case 4, resulting in an increased heat release rate, higher temperature gradient values, and a quicker combustion process.

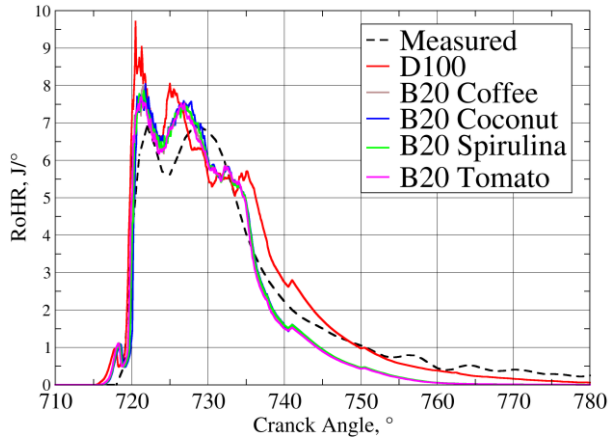

Figure 17: Rate of Heat Release B20 blends – Case 4

4.2. B50 Blends

When mixed in 50% volumetric share, the chemical structure significantly influences the combustion characteristics in all the operating conditions. As illustrated in Figure 18, all biodiesel blends tend to ignite later than the B20 blends, with the coconut oil blend being the latest. As the volumetric share of biodiesel in diesel increases, the chemical structure

tends to impact the combustion process significantly. The more significant disparity is attributed to an even higher content of unsaturated methyl esters containing a higher oxygen share than the shorter-chained saturated methyl esters. This disparity is best exemplified by the 3% higher peak pressure exhibited by the B50 tomato blend compared to the B50 coconut blend. The longer ignition delay time is also visible in the temperature graph. The RoHR demonstrates that the B50 blends have a significantly lower peak value than D100, and the ignition delay time is much more pronounced than in the B20 blends. Additionally, a significant drop in the released energy is observable when examining the expansion cycle, corresponding to markedly lower pressure and temperature values.

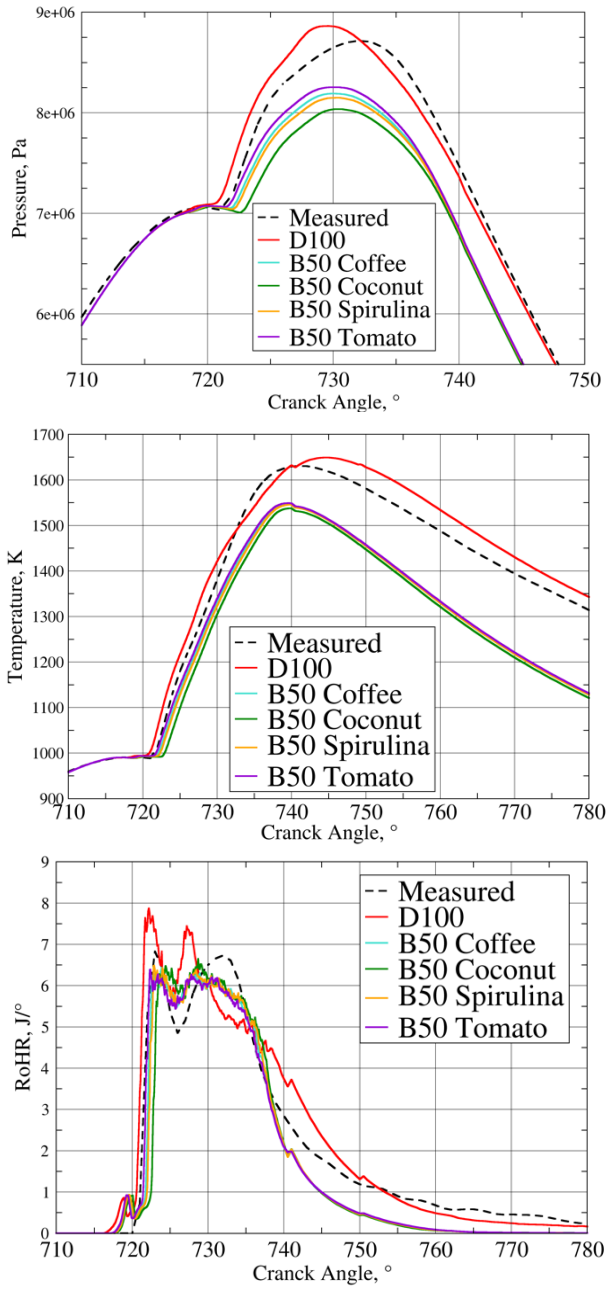

Figure 18: In-cylinder pressure, temperature and RoHR of B50 blends – Case 1

Following the trend of B20 blends, the worst agreement between experimental data and D100 is achieved for Case 2 in Figure 19. In Case 2, the coconut B50 blend with the highest share of saturated FAME ignited last and produced the lowest pressure values as opposed to the highly unsaturated Tomato-seed mixture. Unlike the B20 mixture (Figure 9), the difference in ignition delay time is much more expressed.

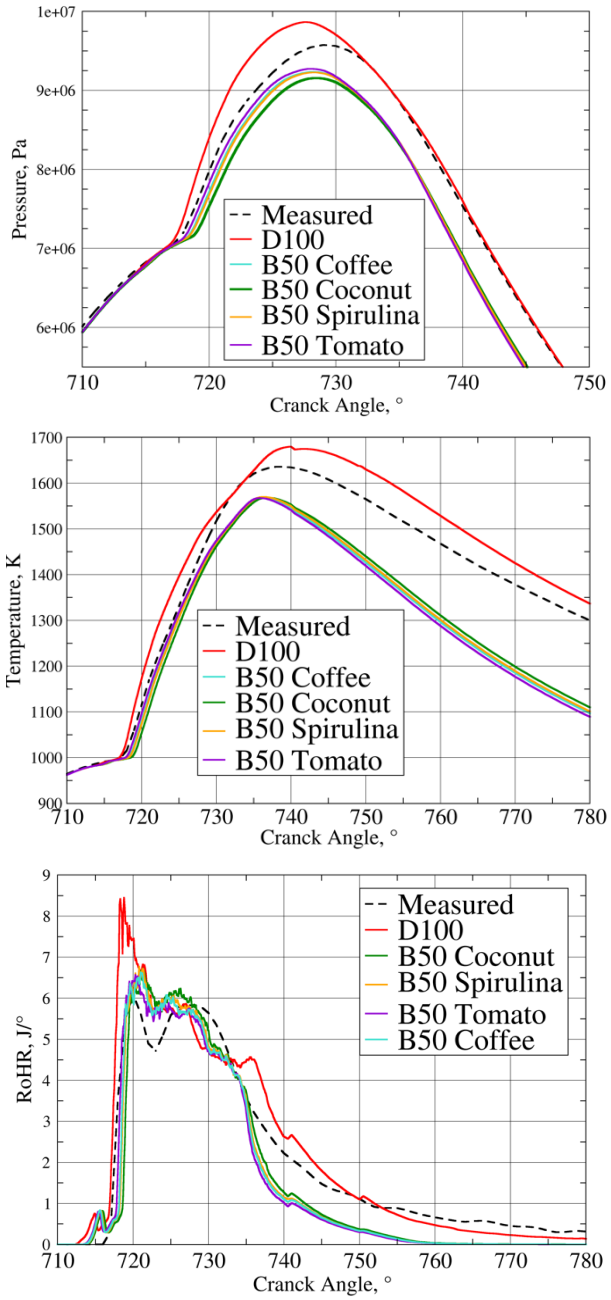

Figure 19: In-cylinder pressure, temperature and RoHR of B50 blends – Case 2

For both B20 and B50 mixtures, the behaviour of Case 3 in Figure 20 is similar, with a very late time of ignition resulting in higher peak values later in the combustion process. The B50 blends exhibit different peak temperature values from Case 1 and Case 2. The longer ignition

delay time for Coconut blends leads to a significant reduction in peak pressure and overall released energy. This, in turn, results in considerably lower pressure and temperature values inside the cylinder, due to the lower values of released energy and the fast drop during the expansion cycle. In terms of the influence of chemical composition, there is an approximately 40 bar difference in peak pressure between the tomato and coconut feedstock.

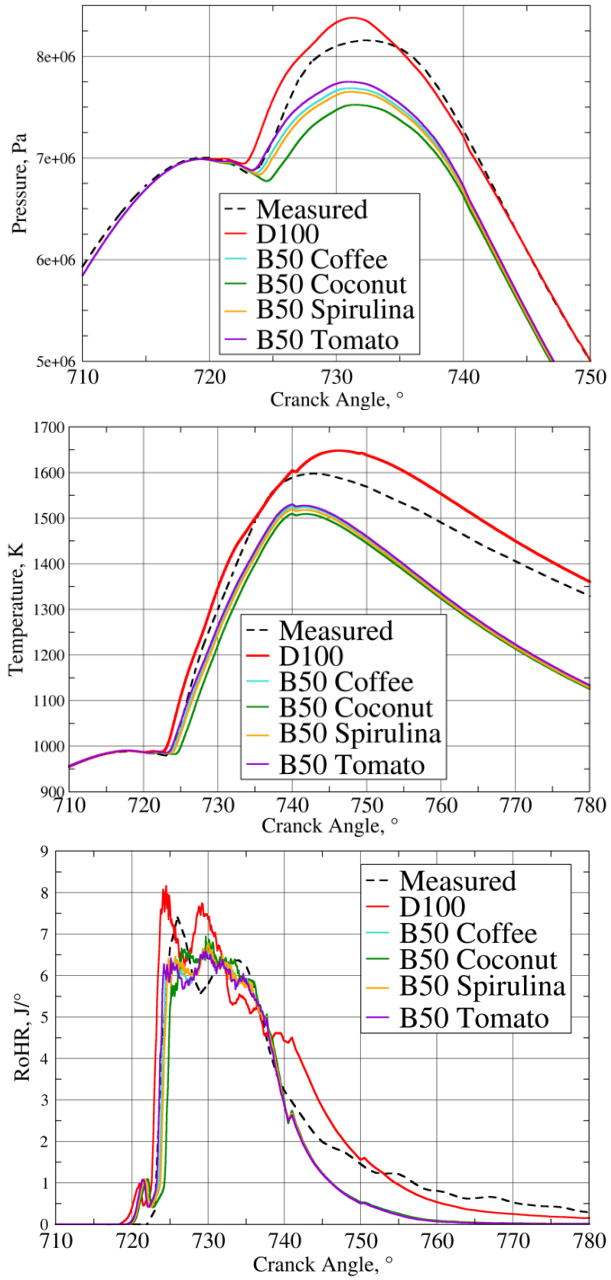

Figure 20: In-cylinder pressure, temperature and RoHR of B50 blends – Case 3

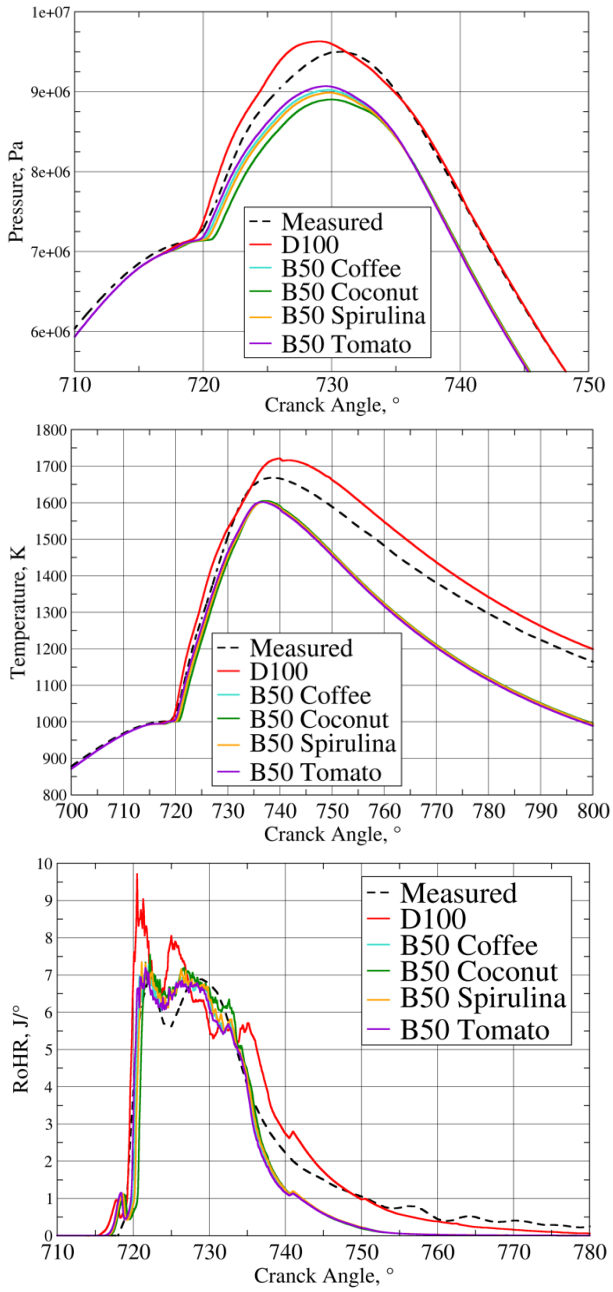

Figure 21: In-cylinder pressure, temperature and RoHR of B50 blends – Case 4

Comparing the peak pressure values of B50 mixtures to D100, an 8.5% reduction was observed. In all the analysed cases, all biodiesel blends showed lower peak pressure and lower released energy than conventional diesel. Released energy can be obtained by calculating the surface under the RoHR graph. A Lower Heating Value (LHV) of conventional diesel fuel is around 43 MJ/kg. Due to its higher oxygen content, biodiesel has lower carbon and hydrogen contents, lowering its mass-energy content by about 10%, depending on the feedstock [51]. By analysing LHV for D100 and Coconut feedstock blends in Case 3, lower values for biodiesel blends were obtained.

Table 12: LHV values for D100 and Coconut oil mixtures – Case 3

	Measured	D100	B20 Coconut	B50 Coconut
LHV [MJ/kg]	43.3	45.3	37.8	32.3

Due to its lower mass energy values, the energy content decreases by increasing the share of biodiesel in the diesel-biodiesel blends. This trend is visible in Table 12. However, the computed values are somewhat lower compared to the literature. The usage of surrogate species can justify this behaviour as the mass fraction of oxygen decreases by increasing the carbon chain of fatty acids, and the heating value increases [52]. Due to these actions, short-chained surrogates MD ($C_{11}H_{22}O_2$) and MD9D ($C_{11}H_{20}O_2$) exploit lower heating values. Additionally, since the pressure within the cylinder is influenced by the proportion of fuel combusting during the premixed stage and its capacity to mix effectively with the air in the combustion chamber, the high viscosity and low volatility of biodiesels can lead to inadequate atomization and mixing with air, which consequently lowers pressure values [53].

4.3. Injected mass adaptation

Due to lower values of LHV for biodiesel blends, a smaller amount of energy was released per the same amount of injected fuel. Therefore, an analysis was performed to check whether the combustion characteristics of the experimental fuel could be matched with a diesel-biodiesel mixture by altering its injected fuel.

The released energy can be obtained by calculating the surface under the RoHR curve. The analysis was performed for Case 3 and both coconut oil mixtures, including the n-heptane surrogate (D100). The calculated released energy for 1/8 of a cylinder is $Q_{EXP} = 147.03$ J. By dividing the released energy by an LHV value, a new corrected mass can be obtained, presented in Table 13. The following equation was applied to obtain injected mass adaptation.

$$m_{corr} = \frac{Q_{EXP}}{LHV} \tag{16}$$

Table 13 shows that a 4% reduction in injected mass for a 14.6% increase in the injected fuel mass was gained for B20, and a 34% increase in the injected fuel mass was gained for B50.

Table 13: Injected fuel mass correction for the diesel fuel, and biodiesel blends

Injected fuel mass	(kg)
$m_{D100_{corr}}$	$3.25 \cdot 10^{-6}$
$m_{B20_{corr}}$	$3.89 \cdot 10^{-6}$
$m_{B50_{corr}}$	$4.55 \cdot 10^{-6}$

Figure 22 shows the obtained values for the B20 coconut oil blend with more fuel injected. It can be seen that the combustion process improved significantly. The combustion process is more intensive than the experimental fuel, with higher peak values in all the characteristics. The ignition delay time is the same as the observed values, but when ignition

occurs, it is more rapid, as seen from the slightly higher pressure and temperature gradients. Also, a higher pressure during the expansion cycle corresponds to higher amounts of released energy. An 8% increase in peak pressure values was obtained compared to the B20 values with lower mass injected. For the D100 case, a decrease in overall performance is noted due to reduced injected fuel. Slightly lower pressure values are observed due to lower amounts of released energy.

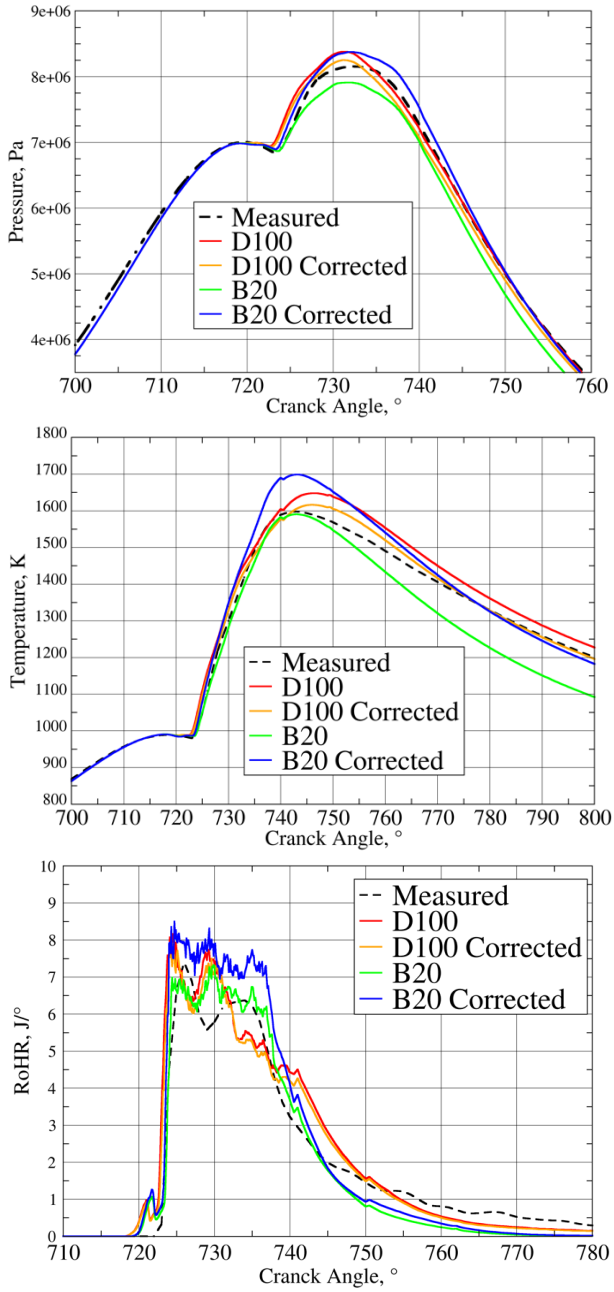

Figure 22: In-cylinder pressure, temperature and RoHR for B20 blends with corrected injected mass – Case 3

Figure 23 exhibits a similar pattern for the B50 blend, with superior combustion achieved as evidenced by higher peak pressure and RoHR values. The RoHR peak value significantly increases with more significant amounts of biodiesel injected into the combustion chamber. This phenomenon can be attributed to the higher oxygen content in the fuel, leading to more complete combustion within the cylinder. In the case of the B50 Coconut blend, the peak pressure increased by 16% when the fuel injection mass was raised.

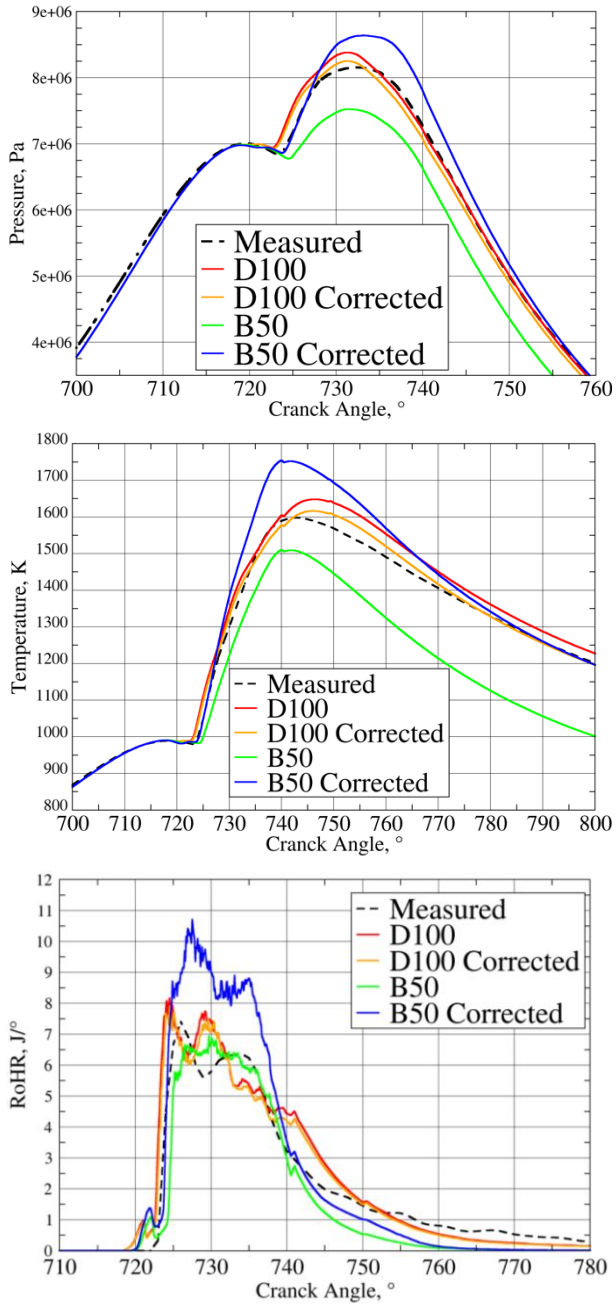

Figure 23: In-cylinder pressure, temperature and RoHR for B50 blends with corrected injected mass – Case 3

The lower mass energy of biodiesel necessitates a greater fuel injection rate to achieve combustion characteristics comparable to conventional diesel. The increase in injected fuel mass required is directly proportional to the volumetric fraction of biodiesel in the fuel blend, and may reach up to 34%. In the present study, both coconut blends exhibited satisfactory behavior during compression and expansion cycles. Nevertheless, the ignition process yielded approximately 10 bar higher pressure values, which may be modified by adjusting certain simulation parameters.

4.4. Temperature distribution

The following chapter will look at the temperature field of a single operating point. Side-to-side comparison of temperature fields for all generation feedstocks in the B20 share will be analysed first. Then a single feedstock will be compared in B20 and B50 shares, respectfully. WCGO blends were not observed, as their behaviour is similar to the Spirulina blend.

The temperature field for Case 3 is shown in Figure 24. When the fuel is injected into the pressurised gas mixture, it is injected at a lower temperature than the gas inside the combustion chamber. Since the fuel is injected in liquid form, the energy necessary for the latent heat of vaporization is transferred from the internal energy of the gasses inside the cylinder. Therefore, the cooling of the gas phase is visible at around 720 CA°. Due to higher temperature conditions, the evaporated fuel ignites, and the combustion process commences at the periphery of the spray vapour cloud, as seen at around 732 CA°. A significant difference is visible around the spray vapour as the flame starts to consume the evaporated fuel. It can be noticed that for the D100 fuel, at 732 CA°, almost all the fuel ignited, whereas, for the B20 blends, a significant share of the injected fuel is still not ignited. When only looking at the B20 blends, it can be seen that the combustion process in the tomato-seed mixture diffused much further toward the injection point than in the coconut oil mixture. This behaviour corresponds to Figure 12, where we can see a shorter ignition delay time for tomato-seed oil. Later, at around 744 CA°, due to turbulent behaviour inside the combustion chamber, the fuel vapour diffuses away from the spray axis and moves towards the compensational volume where the highest temperatures are found.

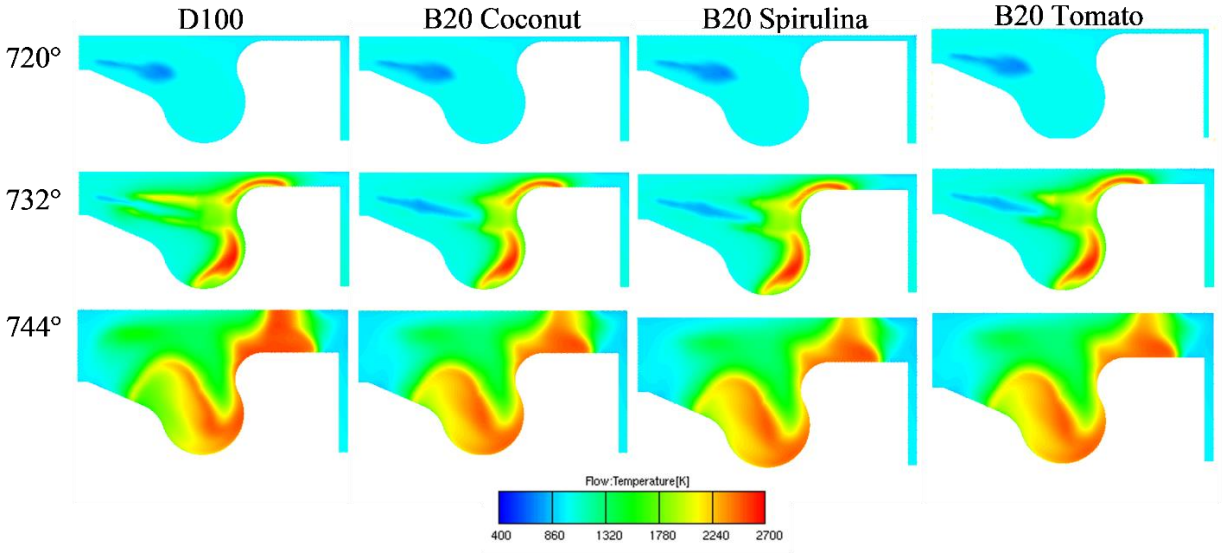

Figure 24: Temperature field for B20 blends - Case 3

Figure 25 shows the temperature field for B20 and B50 blends of coconut oil. There are visible differences in the two blends, as the temperature field is much lower for the B50 blend showing good agreement with the pressure and RoHR values analysed previously. Around 720 CA°, no noticeable differences are seen. However, at 732 CA°, less fuel is ignited in the higher-volume mixture. Later in the combustion process, much lower peak temperature areas are observed.

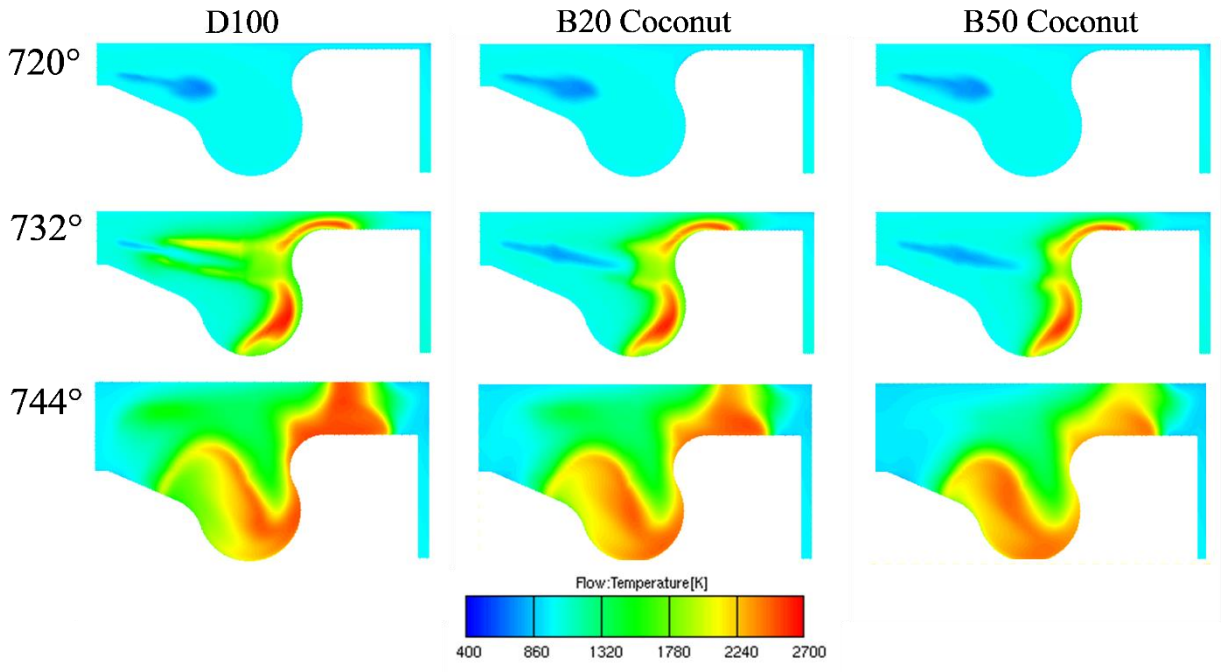

Figure 25: Temperature field for Coconut oil blends - Case 3

Figure 26 shows the temperature field for the corrected amount of injected fuel. Significant differences are observed. An enormous cloud of lower temperature is formed during injection, suggesting more fuel is injected inside the cylinder. As seen in Figure 22, more intense combustion occurs with higher temperature values. Generally, more uniform combustion occurs throughout the cylinder when fuel and air are mixed more efficiently.

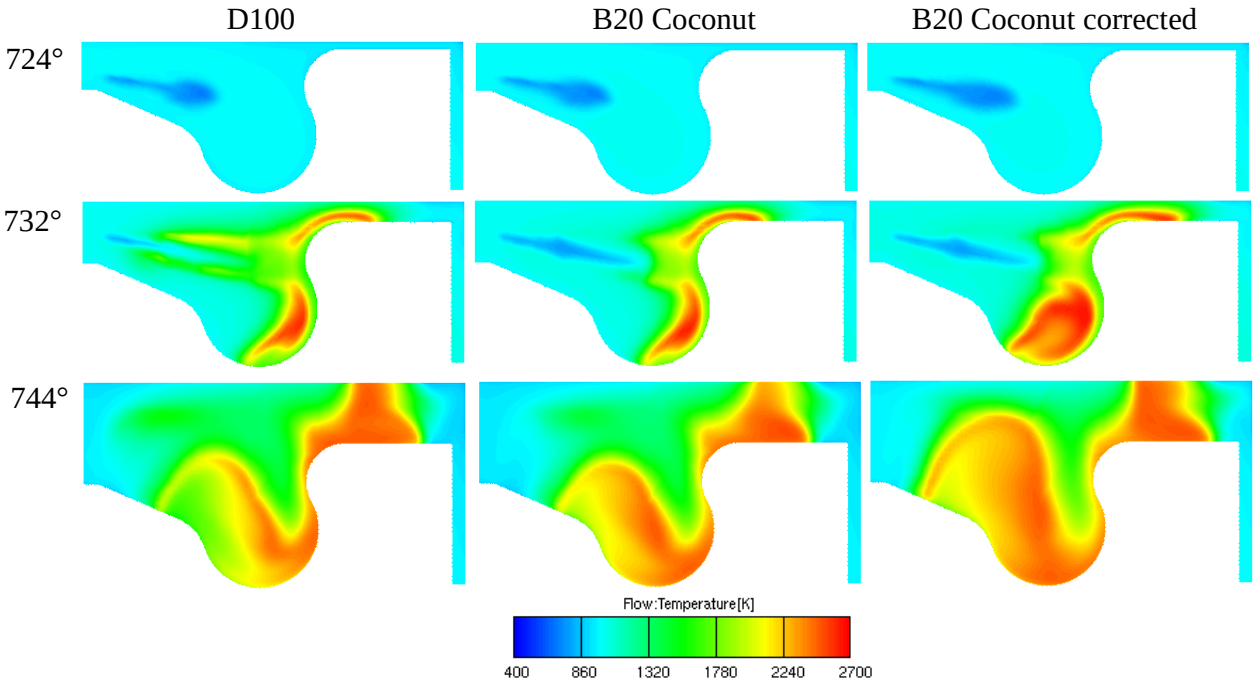

Figure 26: Temperature comparison for a different amount of injected B20 Coconut oil fuel - Case 3

The B50 blend of Coconut oil in Figure 27 is shown with a higher fuel injection quantity that exhibits behavior similar to that of the B20 blend. An increased fuel injection amount generates an immense cloud of lower temperature. As combustion commences, higher temperatures are produced within the piston bowl. During expansion, a more uniform temperature field is formed compared to D100, and B50 blends with lower fuel injection amounts.

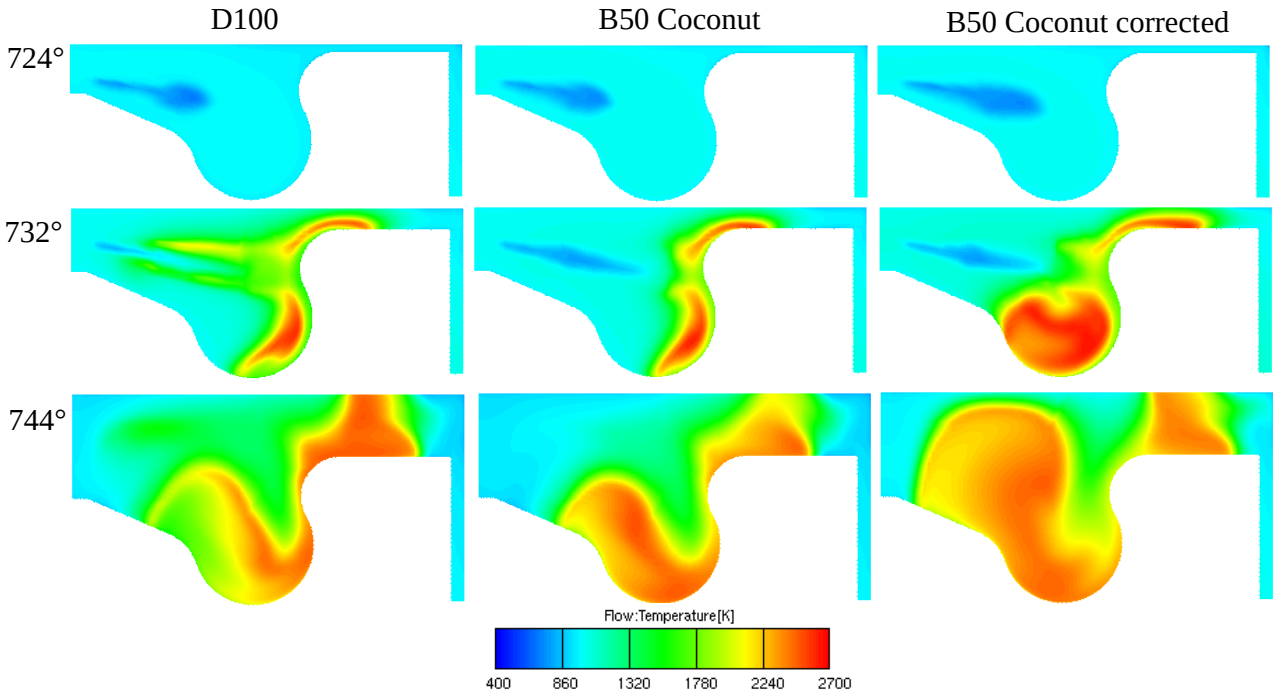

Figure 27: Temperature comparison for a different amount of injected B50 Coconut oil fuel - Case 3

4.5. Autoignition results

The following subsection shows the autoignition timing of evaporated fuel - air mixture between all the simulations. The procedure for determining autoignition timing is inherited from [20]. The inflexion point of the temperature curve was used to distinguish cold and hot flame ignitions and calculate the main ignition timing. The employed procedure is shown in Figure 28. The autoignition results are shown in Figure 29, which correlate with the RoHR diagrams, in which the sudden increase in the gradient indicates autoignition of evaporated fuel - air mixture. From the presented results, it is clear that higher content of MD in biodiesel blends results in postponed ignition, which can be mainly observed for coconut cases, where the content of MD is the highest compared to the other biodiesel blends. Additionally, the autoignition timing between cases is not preserved for each fuel. It can be seen that for the earliest injection in Case 2, the high-content biodiesel blends B50, had delayed ignition compared to the other cases, which can be attributed to the higher reaction energy of MD chemical species. The minor autoignition delay is obtained as expected for injection at the latest injection and close to the top dead centre. Finally, the ignition delay times agree with the pressure curvatures in Figure 6.

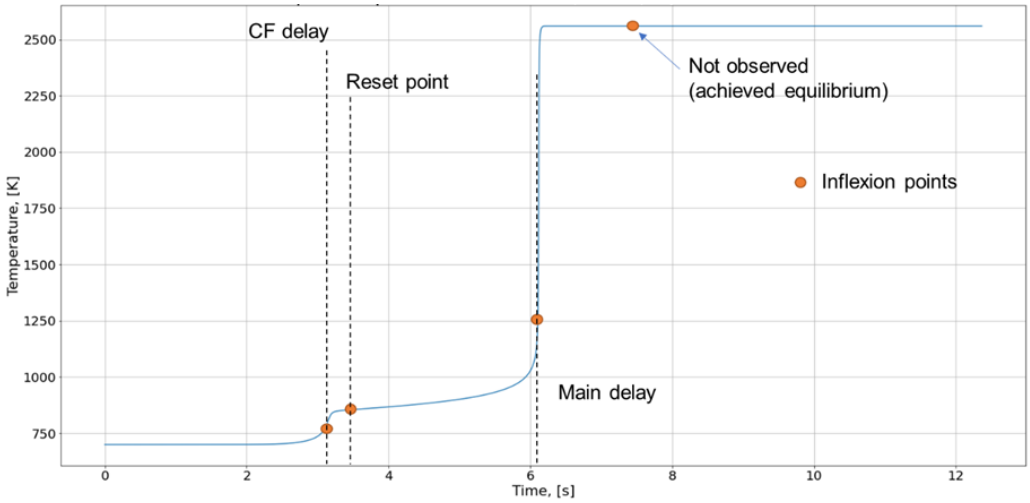

Figure 28: Autoignition timing calculation based on inflexion points

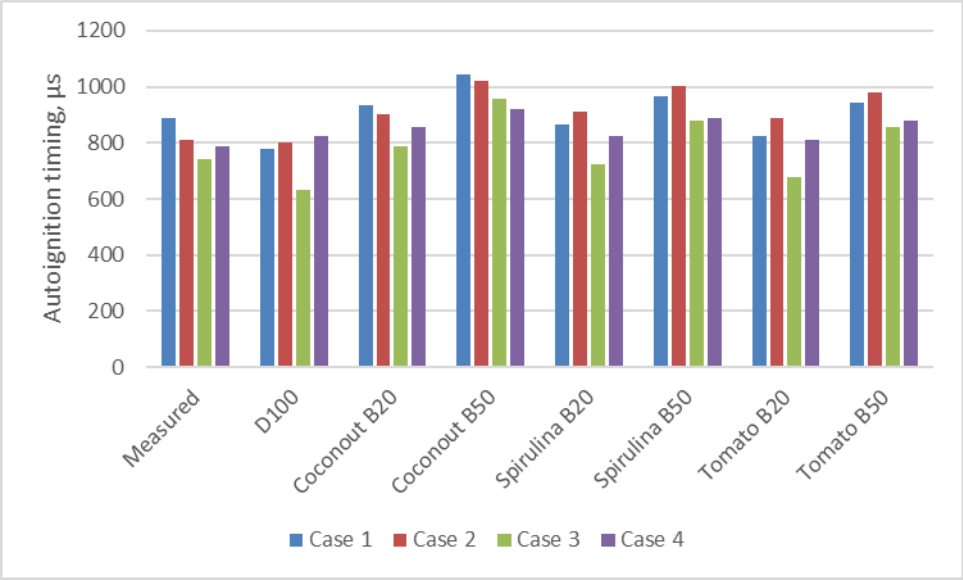

Figure 29: Autoignition timing for all observing cases

4.6. NO emissions results

NO_x pollutants are formed around the flame region under high-temperature conditions, with higher temperatures and higher flame propagation rates. Compression ignition engines highly contribute to NO_x emissions due to higher temperatures achieved inside the combustion chamber than other ICE types. During diesel combustion, NO_x pollutants are predominantly formed in the shape of nitrogen oxide (NO). Considering this, the influence of the other NO_x compounds has been neglected in this work. The mass fraction of NO formed in all operating points under different conditions is shown in Table 14.

Table 14: NO mass fraction in exhaust gases (ppm)

	Measured	D100	B20 Coconut	B50 Coconut	B20 Spirulina	B50 Spirulina	B20 Tomato	B50 Tomato

Case 1	562	407	290	172	298	200	303	224
Case 2	592	497	378	263	384	281	389	294
Case 3	368	262	172	77	177	100	186	120
Case 4	859	663	515	367	523	390	534	414

From the NO profiles in Figure 30, it can be seen that the kinetic mechanism underpredicted NO formation in all the cases for pure diesel (D100). The highest difference of 38% can be observed for Case 1. For the biodiesel blends, the NO formation directly correlates with temperatures, as the higher the temperatures more NO is formed. For Case 3, all the blends emitted the lowest amounts of NO as the peak temperatures were the lowest of all observed cases. On the other hand, Case 4, which showed the most effective combustion of the observed cases, also showed that the highest amounts of NO were formed.

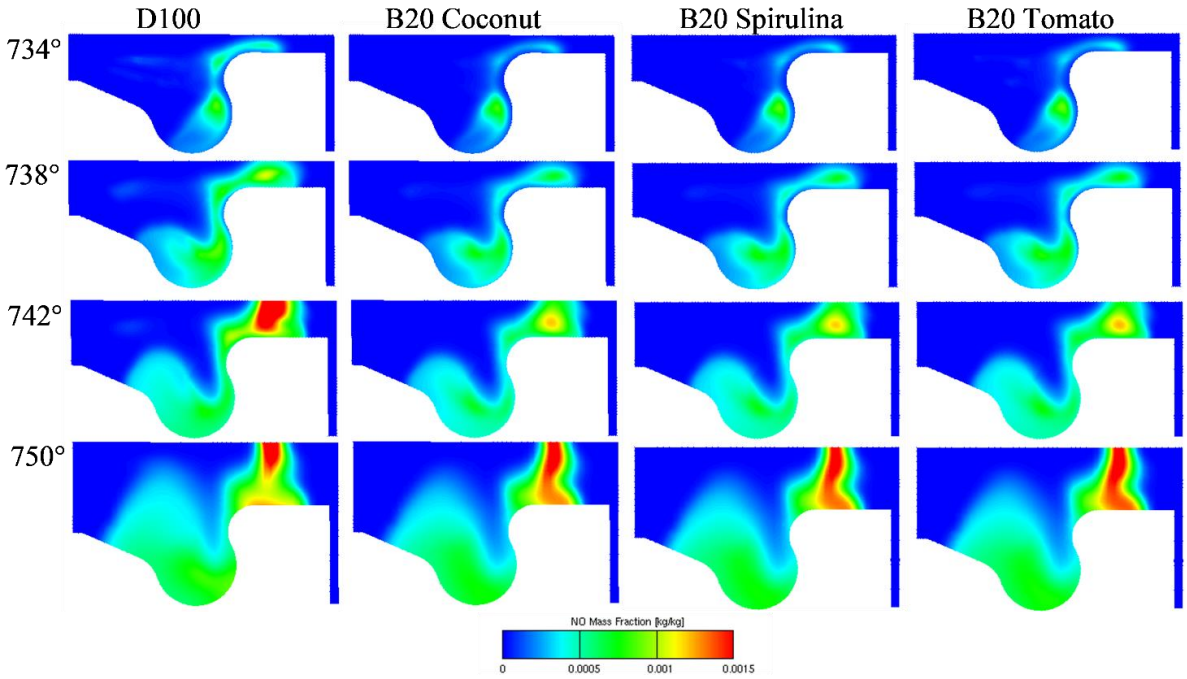

Figure 30: NO mass fraction for B20 blends – Case 3

Table 14 shows that there are numerous similarities in NO formation inside the cylinder among different biodiesel feedstock types. Specifically, all blends exhibit comparable NO content at the end of the cycle. The Tomato blend displays the highest NO fraction, corresponding to marginally elevated temperatures during combustion inside the cylinder. In Figure 30, all B20 blends are compared at the same CA° times. The most significant discrepancy is observed when comparing the blends to D100 fuel, where combustion occurs much more rapidly and at higher temperatures. At 742 CA°, D100 experiences much higher temperatures, as demonstrated by a large NO cloud forming near the cylinder head. This behavior corresponds to the temperature field inside the cylinder depicted in Figure 24, where the highest temperatures are observed near the cylinder head's cylinder walls. Among

different feedstocks, all blends exhibit comparable behavior during combustion. The following figure compares the B20 and B50 blends of Coconut oil.

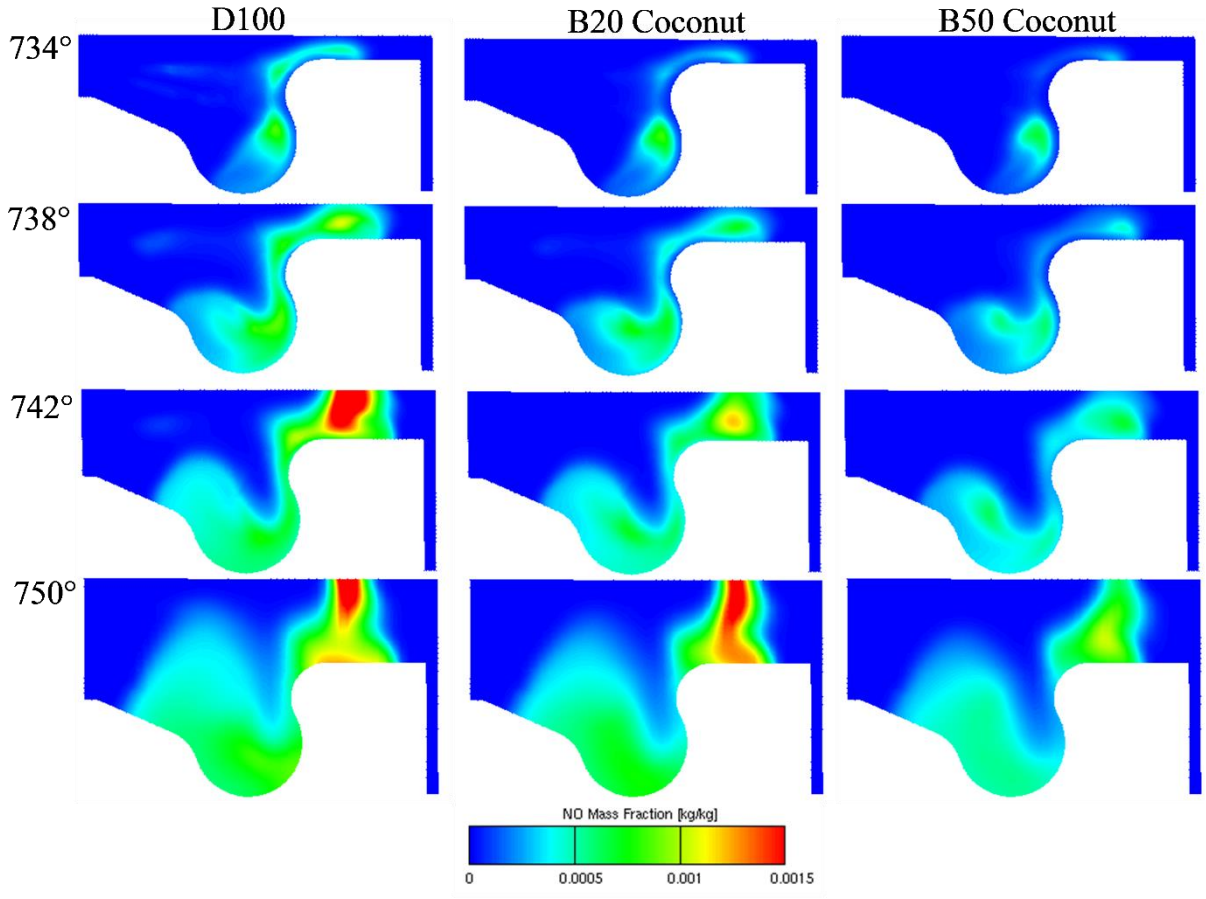

Figure 31: NO mass fraction for Coconut oil blends - Case 3

When comparing the B20 and B50 blends, notable distinctions emerge. The earlier analysis of combustion characteristics revealed that fuels with higher biodiesel fractions tend to undergo delayed ignition and reach lower temperatures, which is also reflected in the NO formation within the cylinder. As a result of the lower temperatures, less NO is produced inside the cylinder. Furthermore, NO emissions for the Coconut oil blends with the corrected mass injected were also analysed. The amount of NO formed during one cycle is shown in Table 15.

Table 15: NO mass fraction from the corrected mass Coconut blends

	Measured	D100	D100 corrected	B20 Coconut	B20 Coconut corrected	B50 Coconut	B50 Coconut corrected
Case 3	368	262	248	172	237	77	245

Higher amounts of NO are released by trying to obtain similar released energy as the experimental fuel. As shown in Figure 22 and Figure 23, higher temperatures were obtained

in the cylinder for the coconut blends with the corrected mass. Due to these higher local temperatures, more NO is formed in the cylinder. Compared to D100 fuel with the adapted amount of injected fuel, a decrease in NO of 4.6% and 1.2% for B20 and B50 is observed. Figure 32 compares the B20 Coconut blend with different injected fuel masses to D100. Overall, the highest share of NO is found on the outer edges of the cylinder wall, but due to intense combustion, NO is more uniformly dispersed inside the cylinder than D100 and B20 with less fuel injected.

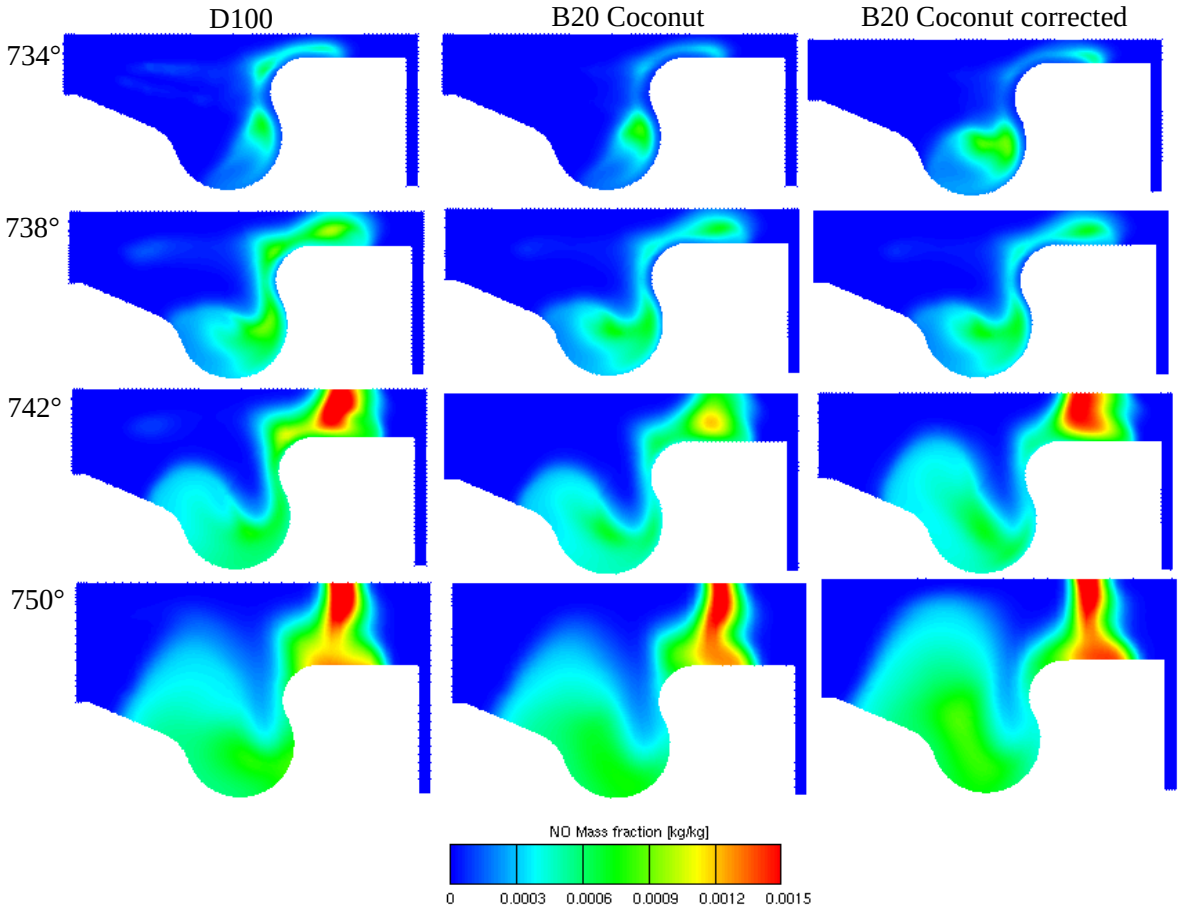

Figure 32: NO mass fraction comparison for a different amount of injected B20 Coconut oil fuel - Case 3

For the B50 coconut blend, the corrected mass showed the best combustion performance resulting in the highest pressure and temperature values. Due to such high temperatures

(Figure 23), good oxidation of nitrogen led to a high share of NO inside the cylinder shown in Figure 33.

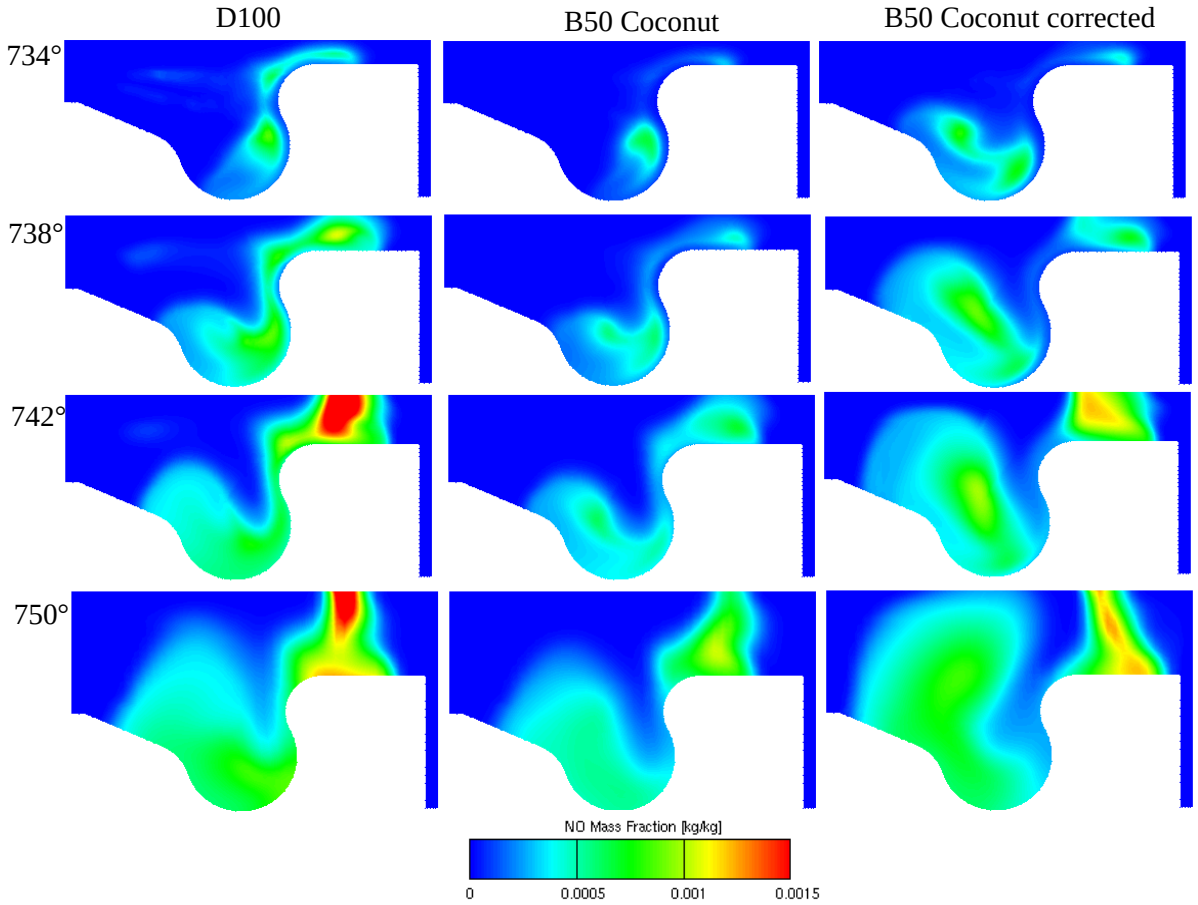

Figure 33: NO mass fraction comparison for a different amount of injected B50 Coconut oil fuel - Case 3

4.7. CO_2 emission

For the analysis of the emitted carbon dioxide, a simple case study was conducted to compare two different approaches for the CO_2 emission analysis. CO_2 emissions obtained via CFD simulations for one operating cycle were compared to yearly CO_2 emissions calculated via the CO_2 emission factor.

4.7.1. Comparison of CO_2 predictions between CFD simulation and emission factors

For the yearly emissions analysis of CO_2, the values of the average mileage and fuel consumption of a diesel-operated car in the European Union were taken from [54] Obtained values are:

Yearly mileage of 19000 kilometres

Fuel consumption of 6.4 l/100 km

By simple conversion, an amount of 1033.6 kg/year of diesel fuel is consumed per vehicle in the European Union.

The CO_2 emissions calculated by the Emission factors methodology are calculated with the following equation:

$$E_{CO_2} = A \cdot LHV \cdot EF_{fuel} \cdot OF \tag{17}$$

where:

E_{CO_2} – CO_2 emissions $[t/year]$ (a ton of CO_2 per year)

A – the amount of consumed fuel $[kg/year]$, (kilogram of fuel per year)

LHV – lower heating value $[MJ/kg]$, (MJ per kilogram of fuel)

EF_{fuel} – emission factor of the specific fuel $[t/MJ]$ (a ton of CO_2 per MJ)

OF – oxidation factor

The fuels LHV are obtained from the analysed biodiesel blends:

Table 16: LHV fuel values

Fuel	LHV [MJ/kg]
D100	45.29
B20 Coconut	37.83
B50 Coconut	32.34
B20 Tomato	37.71
B50 Tomato	32.95
B20 Coffee	37.91
B50 Coffee	32.84
B20 Spirulina	37.68
B50 Spirulina	32.60

The emission factor for diesel and biodiesel were acquired from the Intergovernmental Panel on Climate Change (IPCC) database:

Table 17: Emission factors for Diesel and Biodiesel

Fuel	EF [t CO_2/TJ]
Diesel	74.1
Biodiesel	76.8

By applying IPCC guidelines, the value of the oxidation factor is 1, which implies that all the carbon inside the fuel is burnt.

Finally, yearly CO_2 emissions for individual blends are obtained:

Table 18: Yearly emissions of CO_2 for analysed blends

Fuel	E_{CO2} [t/year]
D100	3.466
B20 Coconut	2.936
B50 Coconut	2.564

B20 Tomato	2.906
B50 Tomato	2.584
B20 Coffee	2.975
B50 Coffee	2.557
B20 Spirulina	2.925
B50 Spirulina	2.585

Results show an approximate 15% reduction in CO_2 emissions when burning the same amount of B20 diesel-biodiesel fuels compared to plain diesel (D100). For the B50 blends, a 26% reduction is achieved.

4.7.2. Simulated CO_2 emissions

With the CFD simulations, CO_2 emissions were analysed after a complete operating cycle. This approach can obtain more precise values as direct amounts of hazardous gasses formed during combustion can be measured. CO_2 mass fractions at 860 CA° for Case 3 are shown in Table 19.

Table 19: Share of CO_2 in residual gases – Case 3

Fuel	Mass fraction [kg/kg]
D100	0.1094
B20 Coconut	0.0970
B50 Coconut	0.0870
B20 Tomato	0.0970
B50 Tomato	0.0888
B20 Coffee	0.0973
B50 Coffee	0.0880
B20 Spirulina	0.0969
B50 Spirulina	0.0878

B20 blends showed a reduction of approximately 11% in emitted CO_2 compared to conventional fuel, whereas B50 mixtures reduced CO_2 emission by 20%.

A comparison between the two approaches was conducted. Figure 34 and Figure 35 show a relative comparison of diesel-biodiesel blends to conventional fuel (D100) for both methods.

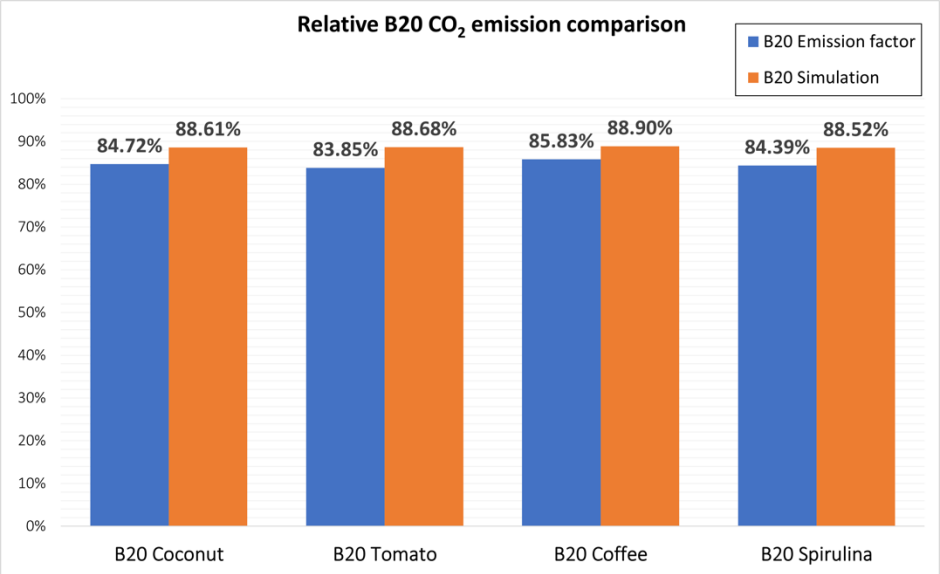

Figure 34: Relative B20 CO_2 emission comparison

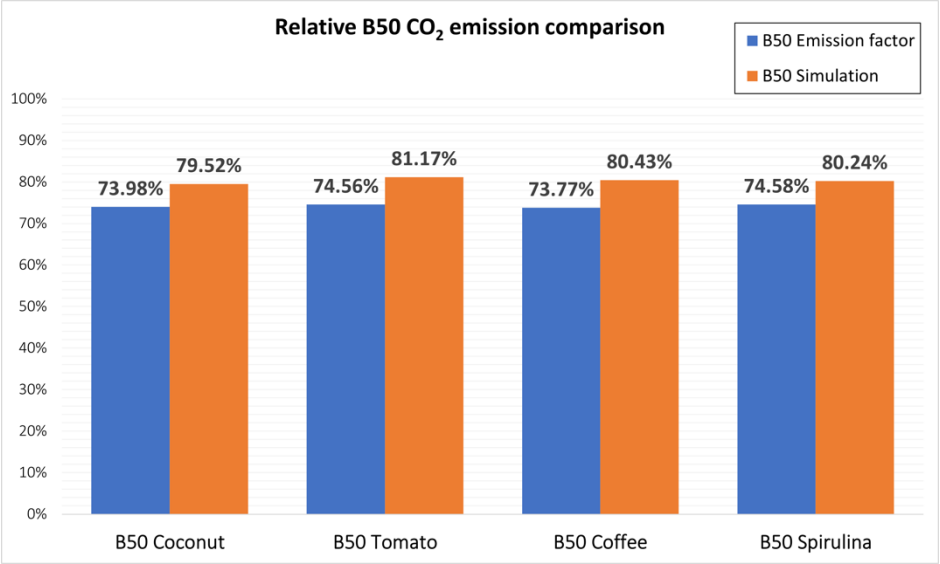

Figure 35: Relative B50 CO_2 emission comparison

Calculating CO_2 emission using the Emission factor method records slightly higher CO_2 reductions across all the fuel blends. Nevertheless, considering the two methods showed similar CO_2 emissions, the Emission factor approach can give a good approximation for the diesel-biodiesel blends quickly. However, a CFD analysis of in-cylinder combustion is advised for a more in-depth view of the composition of exhaust gasses, as many engine parameters can be altered, leading to a detailed insight into exhaust gasses.

5. CONCLUSION

In this paper, a CFD combustion analysis using chemical kinetics for different generations of Biodiesel and its blends was performed. Biodiesel, due to its similar physical properties to conventional diesel, is highly applicable in ICE when blended with traditional diesel. Also, being CO_2 neutral makes it an attractive alternative for replacing standard fossil fuels. Four different plant-derived feedstocks in B20 and B50 blends were analysed in CFD software AVL-FIRE™ in four operating points, where combustion characteristics such as in-cylinder pressure, temperature, and rate of heat release were analysed and compared to experimental data. A reduced chemical mechanism capable of depicting biodiesel behaviour via two species surrogates was used. The mechanism consisted of 115 species and 460 chemical reactions.

The comparison to the experimental data showed good agreement during the compression and expansion period. However, shorter ignition delay times and slightly higher peak values were obtained in all the operating points, which can be attributed to the fuel being depicted by surrogate species. B20 and B50 biodiesel blends showed lower values for all combustion characteristics when the same amount of fuel was injected. This behaviour was due to lower LHV for Biodiesel, implying that more fuel must be injected to reach the same amounts of released energy per cycle. Based on the presented validation results, it can be concluded that the mechanism significantly better describes processes with injection near the top dead center. A reduction in NO_x was also observed for diesel-biodiesel blends compared to conventional diesel.

Based on the findings, it can be concluded that a higher fraction of MD in biodiesel blends causes an autoignition delay, which is particularly noticeable in coconut cases, where MD content is relatively high. The B50 blends that feature a high biodiesel fraction demonstrated delayed ignition compared to other biodiesel, which can be attributed to the elevated reaction energy of MD chemical species.

For the CO_2 emissions, a comparison between CFD simulations and the Emission factor method was conducted. By calculating the emissions by the Emission factor method, slightly higher CO_2 reductions are noted. For large-scale cases, where a quick approximation is needed, the Emission factor can offer a good CO_2 approximation. However, for a more detailed analysis of CO_2 emissions and exhaust gasses in general, CFD simulations can offer a more precise and in-depth analysis of specific fuel emissions.

Concerning the chemical structure of the analysed feedstock, waste tomato-seed oils have shown to be the best, with good combustion characteristics and reduction in CO_2 and NO_x. Also, it is worth mentioning that second and third-generation biodiesels have an overall positive impact on CO_2 emissions as they are CO_2 neutral. Microalgae biodiesel will be a perfect alternative when it becomes profitable as they have a much shorter harvesting time and a much higher oil content than traditional biodiesel oilseeds.

Finally, it can be stated that combustion analysis using chemical kinetics offers good insight into biodiesel behaviour. With some additional engine parameters optimization and a

detailed chemical mechanism where Biodiesel is not depicted by surrogates, better results can be obtained, and diesel-biodiesel blends can match the behaviour of conventional diesel.

Acknowledgments

This work was funded under the auspice of the European Regional Development Fund, Operational Programme Competitiveness and Cohesion 2014−2020, KK.01.1.1.04.0070. Authors would also wish to thank the CFD development group at AVL-AST, Graz, Austria, for their support and technical discussions during the model development.

References

[1] D. Mendoza-Casseres, G. Valencia-Ochoa, J. Duarte-Forero, Experimental assessment of combustion performance in low-displacement stationary engines operating with biodiesel blends and hydroxy, Thermal Science and Engineering Progress. 23 (2021) 100883. https://doi.org/10.1016/j.tsep.2021.100883.

[2] J. E, Z. Zhang, J. Chen, M. Pham, X. Zhao, Q. Peng, B. Zhang, Z. Yin, Performance and emission evaluation of a marine diesel engine fueled by water biodiesel-diesel emulsion blends with a fuel additive of a cerium oxide nanoparticle, Energy Convers Manag. 169 (2018) 194–205. https://doi.org/10.1016/j.enconman.2018.05.073.

[3] D. Tan, Z. Chen, J. Li, J. Luo, D. Yang, S. Cui, Z. Zhang, Effects of Swirl and Boiling Heat Transfer on the Performance Enhancement and Emission Reduction for a Medium Diesel Engine Fueled with Biodiesel, Processes. 9 (2021) 568. https://doi.org/10.3390/pr9030568.

[4] J. Niemisto, P. Saavalainen, E. Pongracz, R.L. Keiski, Biobutanol as a Potential Sustainable Biofuel - Assessment of Lignocellulosic and Waste-based Feedstocks, Journal of Sustainable Development of Energy, Water and Environment Systems. 1 (2013) 58–77. https://doi.org/10.13044/j.sdewes.2013.01.0005.

[5] M.A. Dias, A.S. Haddad, J.N. Souza, A Pathway to Energy and Food Security with Biodiesel, Journal of Sustainable Development of Energy, Water and Environment Systems. 4 (2016) 242–261. https://doi.org/10.13044/j.sdewes.2016.04.0020.

[6] M. Muhammed Niyas, A. Shaija, Biodiesel production from coconut waste cooking oil using novel solar powered rotating flask oscillatory flow reactor and its utilization in diesel engine, Thermal Science and Engineering Progress. 40 (2023) 101794. https://doi.org/10.1016/j.tsep.2023.101794.

[7] V. Krishna Kolli, S. Gadepalli, J. Deb Barma, M. Krishna Maddali, S. Barathula, N. Kumar reddy Siddavatam, Establishment of lower exhaust emissions by using EGR coupled low heat loss diesel engine with fuel blends of microalgae biodiesel-oxygenated additive DEE-antioxidant DPPD, Thermal Science and Engineering Progress. 13 (2019) 100401. https://doi.org/10.1016/j.tsep.2019.100401.

[8] B.D. Wahlen, M.R. Morgan, A.T. McCurdy, R.M. Willis, M.D. Morgan, D.J. Dye, B. Bugbee, B.D. Wood, L.C. Seefeldt, Biodiesel from Microalgae, Yeast, and Bacteria: Engine Performance and Exhaust Emissions, Energy & Fuels. 27 (2013) 220–228. https://doi.org/10.1021/ef3012382.

[9] M.M. Rahman, S. Stevanovic, M.A. Islam, K. Heimann, M.N. Nabi, G. Thomas, B. Feng, R.J. Brown, Z.D. Ristovski, Particle emissions from microalgae biodiesel combustion and their relative oxidative potential, Environ Sci Process Impacts. 17 (2015) 1601–1610. https://doi.org/10.1039/C5EM00125K.

[10] E.G. Giakoumis, C.D. Rakopoulos, A.M. Dimaratos, D.C. Rakopoulos, Exhaust emissions of diesel engines operating under transient conditions with biodiesel fuel blends, Prog Energy Combust Sci. 38 (2012) 691–715. https://doi.org/10.1016/j.pecs.2012.05.002.

[11] J. Sun, J.A. Caton, T.J. Jacobs, Oxides of nitrogen emissions from biodiesel-fuelled diesel engines, Prog Energy Combust Sci. 36 (2010) 677–695. https://doi.org/10.1016/j.pecs.2010.02.004.

[12] H. Mikulčić, J. Baleta, J.J. Klemeš, Cleaner technologies for sustainable development, Clean Eng Technol. 7 (2022) 100445. https://doi.org/10.1016/j.clet.2022.100445.

[13] S.A. Ahmed, S. Zhou, Y. Zhu, Y. Feng, A. Malik, N. Ahmad, Influence of Injection Timing on Performance and Exhaust Emission of CI Engine Fuelled with Butanol-Diesel Using a 1D GT-Power Model, Processes. 7 (2019) 299. https://doi.org/10.3390/pr7050299.

[14] H. Mikulčić, J. Baleta, Z. Zhang, J.J. Klemeš, Sustainable development of energy, water and environmental systems in the changing world, J Clean Prod. 390 (2023) 135945. https://doi.org/10.1016/j.jclepro.2023.135945.

[15] U. Rajak, P. Nashine, P.K. Chaurasiya, T.N. Verma, D.K. Patel, G. Dwivedi, Experimental & predicative analysis of engine characteristics of various biodiesels, Fuel. 285 (2021) 119097. https://doi.org/10.1016/j.fuel.2020.119097.

[16] F. Jurić, P.J. Coelho, P. Priesching, N. Duić, S. Honus, M. Vujanović, Implementation of the spectral line-based weighted-sum-of-gray-gases model in the finite volume method for radiation modeling in internal combustion engines, Int J Energy Res. (2022). https://doi.org/10.1002/er.8177.

[17] H. An, W.M. Yang, J. Li, Effects of ethanol addition on biodiesel combustion: A modeling study, Appl Energy. 143 (2015) 176–188. https://doi.org/10.1016/j.apenergy.2015.01.033.

[18] İ. Temizer, The combustion analysıs and wear effect of biodiesel fuel used in a diesel engine, Fuel. 270 (2020) 117571. https://doi.org/10.1016/j.fuel.2020.117571.

[19] L. Lešnik, B. Vajda, Z. Žunič, L. Škerget, B. Kegl, The influence of biodiesel fuel on injection characteristics, diesel engine performance, and emission formation, Appl Energy. 111 (2013) 558–570. https://doi.org/10.1016/j.apenergy.2013.05.010.

[20] F. Jurić, M. Ban, P. Priesching, C. Schmalhorst, N. Duić, M. Vujanović, Numerical modeling of laminar flame speed and autoignition delay using general fuel-independent function, Fuel. 323 (2022). https://doi.org/10.1016/j.fuel.2022.124432.

[21] A. Arad, E. Sher, G. Enden, Phenomenological soot modeling with solution mapping optimization of biodiesel-diesel blends in diesel engines, Thermal Science and Engineering Progress. 18 (2020) 100544. https://doi.org/10.1016/j.tsep.2020.100544.

[22] D. Kumar Singh, R. Raj, J.V. Tirkey, Performance and emission analysis of triple fuelled CI engine utilizing producer gas, biodiesel and diesel: An optimization study using response surface methodology, Thermal Science and Engineering Progress. 36 (2022) 101486. https://doi.org/10.1016/j.tsep.2022.101486.

[23] S.R. Amini Niaki, S. Mahdavi, J. Mouallem, Experimental and simulation investigation of effect of biodiesel-diesel blend on performance, combustion, and emission characteristics of a diesel engine, Environ Prog Sustain Energy. 37 (2018) 1540–1550. https://doi.org/10.1002/ep.12845.

[24] U. Rajak, T. Subhaschandra Singh, T. Nath Verma, P. Kumar Chaurasiya, S. Shaik, A. Afzal, E. Cuce, A.A. Rajhi, C. Ahamed Saleel, Experimental and parametric studies on the effect of waste cooking oil methyl ester with diesel fuel in compression ignition engine, Sustainable Energy Technologies and Assessments. 53 (2022) 102705. https://doi.org/10.1016/j.seta.2022.102705.

[25] U. Rajak, T.N. Verma, Effect of emission from ethylic biodiesel of edible and non-edible vegetable oil, animal fats, waste oil and alcohol in CI engine, Energy Convers Manag. 166 (2018) 704–718. https://doi.org/10.1016/j.enconman.2018.04.070.

[26] Y. Zhang, Y. Zhong, J. Wang, D. Tan, Z. Zhang, D. Yang, Effects of Different Biodiesel-Diesel Blend Fuel on Combustion and Emission Characteristics of a Diesel Engine, Processes. 9 (2021) 1984. https://doi.org/10.3390/pr9111984.

[27] A. Hossain, D. Smith, P. Davies, Effects of Engine Cooling Water Temperature on Performance and Emission Characteristics of a Compression Ignition Engine Operated with Biofuel Blend, Journal of Sustainable Development of Energy, Water and Environment Systems. 5 (2017) 46–57. https://doi.org/10.13044/j.sdewes.d5.0132.

[28] M. Costa, M. la Villetta, N. Massarotti, D. Piazzullo, V. Rocco, Numerical analysis of a compression ignition engine powered in the dual-fuel mode with syngas and biodiesel, Energy. 137 (2017) 969–979. https://doi.org/10.1016/j.energy.2017.02.160.

[29] D. Piazzullo, M. Costa, Z. Petranovic, M. Vujanovic, M. La Villetta, C. Caputo, D. Cirillo, CFD modelling of a spark ignition internal combustion engine fuelled with syngas for a mCHP system, Chem Eng Trans. 65 (2018) 13–18. https://doi.org/10.3303/CET1865003.

[30] E. Ranzi, A. Frassoldati, A. Stagni, M. Pelucchi, A. Cuoci, T. Faravelli, Reduced Kinetic Schemes of Complex Reaction Systems: Fossil and Biomass-Derived Transportation Fuels, Int J Chem Kinet. 46 (2014) 512–542. https://doi.org/10.1002/kin.20867.

[31] S. Sukumaran, S.-C. Kong, Modelling biodiesel–diesel spray combustion using multicomponent vaporization coupled with detailed fuel chemistry and soot models, Combustion Theory and Modelling. 20 (2016) 913–940. https://doi.org/10.1080/13647830.2016.1199917.

[32] L. Zhang, X. Ren, Z. Lan, A reduced reaction mechanism of biodiesel surrogates with low temperature chemistry for multidimensional engine simulation, Combust Flame. 212 (2020) 377–387. https://doi.org/10.1016/j.combustflame.2019.11.002.

[33] Z. Luo, M. Plomer, T. Lu, S. Som, D.E. Longman, S.M. Sarathy, W.J. Pitz, A reduced mechanism for biodiesel surrogates for compression ignition engine applications, Fuel. 99 (2012) 143–153. https://doi.org/10.1016/j.fuel.2012.04.028.

[34] A. Stagni, C. Saggese, M. Bissoli, A. Cuoci, A. Frassoldati, T. Faravelli, E. Ranzi, Reduced kinetic model of biodiesel fuel combustion, Chem Eng Trans. 37 (2014) 877–882. https://doi.org/10.3303/CET1437147.

[35] V. Józsa, G.T. Hidegh, D. Csemány, R.A. Kardos, C.T. Chong, Dynamics and emission of nearly flameless combustion of waste cooking oil biodiesel in an ultra-low emission non-MILD swirl burner, Fuel. 319 (2022) 123743. https://doi.org/10.1016/j.fuel.2022.123743.

[36] J. Brakora, A Comprehensive Combustion Model for Biodiesel-Fueled Engine Simulations, (2012).

[37] U. Rajak, T.N. Verma, A comparative analysis of engine characteristics from various biodiesels: Numerical study, Energy Convers Manag. 180 (2019) 904–923. https://doi.org/10.1016/j.enconman.2018.11.044.

[38] K. Hanjalić, M. Popovac, M. Hadžiabdić, A robust near-wall elliptic-relaxation eddy-viscosity turbulence model for CFD, Int J Heat Fluid Flow. 25 (2004) 1047–1051. https://doi.org/10.1016/j.ijheatfluidflow.2004.07.005.

[39] F. Juric, M. Vujanovic, Z. Petranovic, Coupling of euler eulerian and euler lagrangian spray methods with chemistry kinetics for modeling of reactive flow and pollutant formation, in: 2021 6th International Conference on Smart and Sustainable Technologies, SpliTech 2021, 2021. https://doi.org/10.23919/SpliTech52315.2021.9566356.

[40] Z. Petranović, T. Bešenić, M. Vujanović, N. Duić, Modelling pollutant emissions in diesel engines, influence of biofuel on pollutant formation, J Environ Manage. 203 (2017) 1038–1046. https://doi.org/10.1016/j.jenvman.2017.03.033.

[41] H.J. Curran, P. Gaffuri, W.J. Pitz, C.K. Westbrook, A Comprehensive Modeling Study of n-Heptane Oxidation, Combust Flame. 114 (1998) 149–177. https://doi.org/10.1016/S0010-2180(97)00282-4.

[42] O. Herbinet, W.J. Pitz, C.K. Westbrook, Detailed chemical kinetic mechanism for the oxidation of biodiesel fuels blend surrogate, Combust Flame. 157 (2010) 893–908. https://doi.org/10.1016/j.combustflame.2009.10.013.

[43] F. Jurić, M. Stipić, N. Samec, M. Hriberšek, S. Honus, M. Vujanović, Numerical investigation of multiphase reactive processes using flamelet generated manifold approach and extended coherent flame combustion model, Energy Convers Manag. 240 (2021). https://doi.org/10.1016/j.enconman.2021.114261.

[44] F. Ma, M.A. Hanna, Biodiesel production: a review1Journal Series #12109, Agricultural Research Division, Institute of Agriculture and Natural Resources, University of Nebraska–Lincoln.1, Bioresour Technol. 70 (1999) 1–15. https://doi.org/10.1016/S0960-8524(99)00025-5.

[45] A. Sander, A. Petračić, J. Parlov Vuković, L. Husinec, From Coffee to Biodiesel—Deep Eutectic Solvents for Feedstock and Biodiesel Purification, Separations. 7 (2020) 22. https://doi.org/10.3390/separations7020022.

[46] R. Karami, M.G. Rasul, M.M.K. Khan, M. Mahdi Salahi, M. Anwar, Experimental and computational analysis of combustion characteristics of a diesel engine fueled with diesel-tomato seed oil biodiesel blends, Fuel. 285 (2021) 119243. https://doi.org/10.1016/j.fuel.2020.119243.

[47] U. Rajak, P. Nashine, T.N. Verma, Characteristics of microalgae spirulina biodiesel with the impact of n-butanol addition on a CI engine, Energy. 189 (2019) 116311. https://doi.org/10.1016/j.energy.2019.116311.

[48] U. Rajak, P. Nashine, T.N. Verma, Assessment of diesel engine performance using spirulina microalgae biodiesel, Energy. 166 (2019) 1025–1036. https://doi.org/10.1016/j.energy.2018.10.098.

[49] D. Chandran, S. Gan, H.L.N. Lau, R. Raviadaran, M. Salim, M. Khalid, Critical relationship between biodiesel fuel properties and degradation of fuel delivery materials of a diesel engine, Thermal Science and Engineering Progress. 7 (2018) 20–26. https://doi.org/10.1016/j.tsep.2018.04.018.

[50] F. Huzjan, F. Jurić, S. Lončarić, M. Vujanović, Deep Learning-based Image Analysis Method for Estimation of Macroscopic Spray Parameters, Neural Comput Appl. 35 (2023) 9535–9548. https://doi.org/10.1007/s00521-022-08184-3.

[51] S.K. Hoekman, A. Broch, C. Robbins, E. Ceniceros, M. Natarajan, Review of biodiesel composition, properties, and specifications, Renewable and Sustainable Energy Reviews. 16 (2012) 143–169. https://doi.org/10.1016/j.rser.2011.07.143.

[52] A. Demirbaş, Fuel properties and calculation of higher heating values of vegetable oils, Fuel. 77 (1998) 1117–1120. https://doi.org/10.1016/S0016-2361(97)00289-5.

[53] M.S. Shehata, Emissions, performance and cylinder pressure of diesel engine fuelled by biodiesel fuel, Fuel. 112 (2013) 513–522. https://doi.org/10.1016/j.fuel.2013.02.056.

[54] G.A. Marrero, J. Rodríguez-López, R.M. González, Car usage, CO2 emissions and fuel taxes in Europe, SERIEs. 11 (2020) 203–241. https://doi.org/10.1007/s13209-019-00210-3.